

RADIATION-HYDRODYNAMIC SIMULATIONS OF COLLAPSE AND FRAGMENTATION IN MASSIVE PROTOSTELLAR CORES

MARK R. KRUMHOLZ¹

Department of Astrophysical Sciences, Princeton University, Princeton, NJ; krumholz@astro.princeton.edu

RICHARD I. KLEIN

Astronomy Department, University of California, Berkeley, CA; and Lawrence Livermore National Laboratory, Livermore, CA;
 klein@astron.berkeley.edu

AND

CHRISTOPHER F. MCKEE

Departments of Physics and Astronomy, University of California, Berkeley, CA; cmckee@astron.berkeley.edu

Received 2006 September 28; accepted 2006 November 4

ABSTRACT

We simulate the early stages of the evolution of turbulent, virialized, high-mass protostellar cores, with primary attention to how cores fragment and whether they form a small or large number of protostars. Our simulations use the Orion adaptive mesh refinement code to follow the collapse from ~ 0.1 pc scales to ~ 10 AU scales, for durations that cover the main fragmentation phase, using three-dimensional gravito-radiation hydrodynamics. We find that for a wide range of initial conditions radiation feedback from accreting protostars inhibits the formation of fragments, so that the vast majority of the collapsed mass accretes onto one or a few objects. Most of the fragmentation that does occur takes place in massive, self-shielding disks. These are driven to gravitational instability by rapid accretion, producing rapid mass and angular momentum transport that allows most of the gas to accrete onto the central star rather than forming fragments. In contrast, a control run using the same initial conditions but an isothermal equation of state produces much more fragmentation, both in and out of the disk. We conclude that massive cores with observed properties are not likely to fragment into many stars, so that, at least at high masses, the core mass function probably determines the stellar initial mass function. Our results also demonstrate that simulations of massive star-forming regions that do not include radiative transfer, and instead rely on a barotropic equation of state or optically thin heating and cooling curves, are likely to produce misleading results.

Subject headings: accretion, accretion disks — equation of state — ISM: clouds — methods: numerical — radiative transfer — stars: formation

Online material: color figures, mpeg animation

1. INTRODUCTION

The previous generation of telescopes revealed a great deal about the gas from which massive stellar clusters form. With them, observers were able to survey the dense clumps of thousands of solar masses that are likely the progenitors of clusters, using molecular line emission (e.g., Plume et al. 1997; Shirley et al. 2003), thermal dust emission (e.g., Carey et al. 2000; Mueller et al. 2002), or infrared absorption (e.g., Menten et al. 2005; Rathborne et al. 2005, 2006; Simon et al. 2006). However, the large distances to these regions, their high extinctions, and the confusion produced by their density prevented these observations from directly probing structures with masses comparable to individual stars, data that have been available since the 1980s for nearby, low-mass star-forming regions. In the last few years, millimeter interferometers and the *Spitzer Space Telescope* have started to change that situation by making available information on the structure of massive star-forming regions comparable to that previously available only for low-mass regions. These observations have identified a population of high-mass cores that are comparable in mass to individual massive stars. They are dense (mean densities $\sim 10^6$ H nuclei cm^{-3} , rising strongly toward their centers), cold (temperatures ≈ 10 – 40 K), turbulent (line widths ~ 1 km s^{-1}),

compact (radii ~ 0.1 pc), and round (aspect ratios of 2:1 or less) (Reid & Wilson 2005; Sridharan et al. 2005; Beuther et al. 2005, 2006; Garay 2005; Pillai et al. 2006). In some cases they show no mid-infrared emission or even mid-infrared absorption, indicating that they have not yet converted a significant fraction of their mass into stars, and are therefore near the onset of star formation.

The idea that these cores might be the progenitors of individual massive stars is bolstered by two pieces of circumstantial evidence. First, the mass function of these cores appears to match the Salpeter (1955) slope of roughly -1.3 in the logarithmic distribution observed for the high-mass end of the stellar initial mass function (IMF, Beuther & Schilke 2004; Reid & Wilson 2005, 2006a, 2006b). This extends earlier observations showing that in nearby low-mass star-forming regions the core mass function matches the IMF as well (Motte et al. 1998; Testi & Sargent 1998; Johnstone et al. 2001; Onishi et al. 2002). Second, cores are mass segregated in such a manner that the mass function is the same throughout a protocluster gas clump, with the exception that the most massive cores, those greater than several solar masses, are found only near the center (Elmegreen & Krakowski 2001; Stanke et al. 2006). Star clusters exhibit a very similar pattern of mass segregation (Hillenbrand & Hartmann 1998; Huff & Stahler 2006), and while some of this may be dynamically produced, much of it is likely a result of the locations

¹ Hubble Fellow.

where the stars formed (Bonnell & Davies 1998; Tan et al. 2006).

However, a direct mapping from core mass to star mass is only possible if massive cores collapse to form individual stars or small multiple systems, as proposed by McKee & Tan (2002, 2003, hereafter MT02 and MT03, respectively), rather than fragmenting into many objects and producing a cluster of low-mass stars. Whether this happens or not is quite uncertain. Bate & Bonnell (2005) argue that dense cores are likely to produce small objects because the Jeans mass decreases with density at fixed temperature (although see Martel et al. 2006). Dobbs et al. (2005) simulate the collapse of massive, turbulent cores and find that they generally fragment into as many as 20 objects, depending on initial conditions and on the assumed gas equation of state. However, Krumholz (2006b) uses one-dimensional analytic calculations to show that radiation feedback from accreting protostars can substantially inhibit fragmentation even at early times, because at the high accretion rates and opacities expected in massive cores, accretion luminosity can heat gas to hundreds of kelvins out to distances of $\gtrsim 1000$ AU from an accreting protostar. Krumholz also finds that using an isothermal or barotropic equation of state, as Bate & Bonnell (2005) and Dobbs et al. (2005) do, is likely to produce misleading results on fragmentation because it misses this effect.

While these calculations are suggestive, because they are analytic, they are necessarily limited in how they deal with real, turbulent cores. The best means of settling the question of how massive cores fragment is direct numerical simulation, including a treatment of radiative feedback from embedded protostars. However, such simulations have not yet been reported in the literature. Some simulations of massive star formation with radiation use quiescent initial conditions (Yorke & Bodenheimer 1999; Yorke & Sonnhalter 2002) in two dimensions and are therefore incapable of answering questions about the fragmentation of turbulent structures. (Those calculations focus on the effects of radiation pressure, an important effect in the later evolution of massive protostars that we do not consider in detail in this paper.) In three dimensions some simulations of massive cores use local cooling functions rather than solving the radiative transfer problem (Banerjee et al. 2006) and are therefore unable to study the effects of feedback. Moreover, the modifications to the cooling function the authors use to approximate the behavior of optically thick gas are of unknown accuracy. Simulations of star formation with feedback and a treatment of radiative transfer have been limited to low-mass, nonturbulent initial conditions (Whitehouse & Bate 2006). Furthermore, both Whitehouse & Bate and Banerjee et al. only advance their simulations to the point where the first collapsed object forms, and for this reason they are incapable of studying accretion and fragmentation or the effects of radiative feedback on either of these processes.

Here, we report the first three-dimensional gravito-radiation hydrodynamic simulations of the collapse and fragmentation of turbulent high-mass protostellar cores. Our simulations include radiative transfer and the effects of feedback from both accretion onto and nuclear burning within embedded protostars. We run through the main fragmentation phase and follow the accretion process to the point where deuterium burning begins in the most massive stars, thereby greatly heating the gas and strongly suppressing further fragmentation. This enables us to address the question of how fragmentation of massive cores proceeds, and how radiative feedback influences it. In § 2 we discuss the methodology for our simulations, and in § 3 we present our results. We discuss the implications of these results for the mechanism

of massive star formation and the origin of the IMF in § 4 and summarize in § 5.

2. SIMULATION METHODOLOGY

2.1. Evolution Equations

We describe the evolution of a massive protostellar core using the equations of gravito-radiation hydrodynamics in the thermal radiation flux-limited diffusion approximation. Written in conservation form, Krumholz et al. (2007) show that these equations to leading order in v/c are

$$\frac{\partial \rho}{\partial t} + \nabla \cdot (\rho \mathbf{v}) = 0, \quad (1)$$

$$\frac{\partial}{\partial t}(\rho \mathbf{v}) + \nabla \cdot (\rho \mathbf{v} \mathbf{v}) = -\nabla P - \rho \nabla \phi - \lambda \nabla E, \quad (2)$$

$$\begin{aligned} \frac{\partial}{\partial t}(\rho e) + \nabla \cdot [(\rho e + P)\mathbf{v}] = & -\rho \mathbf{v} \cdot \nabla \phi \\ & -\kappa_P \rho (4\pi B - cE) + \lambda \mathbf{v} \cdot \nabla E, \end{aligned} \quad (3)$$

$$\begin{aligned} \frac{\partial E}{\partial t} - \nabla \cdot \left(\frac{c\lambda}{\kappa_R} \nabla E \right) = & \sum_i L_i \delta(\mathbf{x} - \mathbf{x}_i) + \kappa_P \rho (4\pi B - cE) \\ & - \lambda \mathbf{v} \cdot \nabla E - \nabla \cdot \left[\frac{3 - R_2}{2} E \mathbf{v} + \frac{3R_2 - 1}{2} E \mathbf{v} \cdot (\mathbf{n}\mathbf{n}) \right], \end{aligned} \quad (4)$$

where ρ , \mathbf{v} , e , and P are the density, velocity, nongravitational specific energy (thermal plus kinetic), and thermal pressure of the gas, respectively, ϕ is the gravitational potential, E is the radiation energy density, $B = ca_R T_g^4/(4\pi)$ is the Planck function of the gas temperature T_g , κ_P is the Planck-mean specific opacity of the gas measured in its rest frame, λ and R_2 are dimensionless numbers describing the radiation field whose significance we discuss below, L_i and \mathbf{x}_i are the luminosity and position of the i th star, and \mathbf{n} is a unit vector antiparallel to ∇E . To leading order in v/c , these equations match those of other flux-limited diffusion radiation-hydrodynamic codes, e.g., ZEUS (Hayes et al. 2006).

The gas pressure, specific energy, and temperature T_g are related by an ideal equation of state

$$P = (\gamma - 1) \left(e - \frac{1}{2} \rho v^2 \right) = \frac{\rho k_B T_g}{\mu}, \quad (5)$$

where $\mu = 2.33m_H$ is the mean particle mass in a gas of molecular hydrogen and helium with the standard cosmic abundance, and we approximate $\gamma = 5/3$, since over most of the volume the gas is too cool to excite rotational or vibrational modes of hydrogen. In practice the choice of γ has almost no effect, because radiative timescales are generally shorter than mechanical ones, so the gas temperature and therefore the effective equation of state is essentially fixed by radiative transfer effects.

The gravitational potential is determined by Poisson's equation, including the contribution from stars, which we treat as point masses,

$$\nabla^2 \phi = 4\pi G \left[\rho + \sum_i M_i \delta(\mathbf{x} - \mathbf{x}_i) \right], \quad (6)$$

where M_i is the mass of the i th star.

The dimensionless numbers appearing in radiation-related terms are the flux limiter λ and the Eddington factor R_2 . Their

purpose is to interpolate between the optically thick and optically thin limits. They are defined by

$$\lambda = \frac{1}{R} \left(\coth R - \frac{1}{R} \right), \quad (7)$$

$$R = \frac{|\nabla E|}{\kappa_R \rho E}, \quad (8)$$

$$R_2 = \lambda + \lambda^2 R^2, \quad (9)$$

where κ_R is the Rosseland-mean specific opacity of the gas. The flux limiter has the property that $\lambda \rightarrow 1/3$ in optically thick regions and $\lambda \rightarrow \kappa_R \rho E / |\nabla E|$ in optically thin regions. For optically thick flows this behavior means that the flux in the frame comoving with the gas approaches $\mathbf{F} \rightarrow -c/(3\kappa_R \rho) \nabla E$, the correct value for diffusion. For optically thin flows it limits to $\mathbf{F} \rightarrow c \mathbf{E} \mathbf{n}$, so that the effective propagation speed of the radiation is limited to c . Similarly, for optically thick regions $R_2 \rightarrow 1/3$, which sets the comoving-frame radiation pressure tensor to the correct isotropic behavior, $\mathcal{P} \rightarrow (E/3)\mathbf{I}$, where \mathbf{I} is the identity tensor. For optically thin flows $R_2 \rightarrow 1$, which gives $\mathcal{P} \rightarrow E \mathbf{n} \mathbf{n}$, the correct limiting value for free-streaming radiation. We refer readers to Krumholz et al. (2007) for a detailed treatment of the relationship between the comoving frame and lab frame quantities, and how the values of λ and R_2 are related to comoving frame quantities.

Our equations are easy to understand intuitively. The term $-\lambda \nabla E$ in the momentum equation (eq. [2]) simply represents the radiation force $\kappa_R \rho \mathbf{F}/c$, neglecting distinctions between the comoving and laboratory frames that are smaller than order v/c . Similarly, the terms $-\kappa_P \rho (4\pi B - cE)$ and $\lambda \mathbf{v} \cdot \nabla E$ in the gas energy equation (eq. [3]) represent radiation absorbed minus radiation emitted by the gas, and the work done by the radiation field on the gas. In the radiation energy equation (eq. [4]), the second term on the left-hand side is the divergence of the radiation flux, i.e., the rate at which radiation diffuses, and the terms on the right-hand side describe, from left to right, radiation emitted by protostars, radiation emitted minus radiation absorbed by gas, work done by the gas on the radiation field, and advection of radiation enthalpy by the gas.

Note that our equations correspond to those of Krumholz et al. (2007) for the static diffusion case, which Krumholz et al. show is the relevant limit for massive protostellar envelopes, with two differences. First is the addition of the terms describing gravity and point sources of radiation, which Krumholz et al. do not include. Second is a difference in the coefficient of the work term, $\lambda \mathbf{v} \cdot \nabla E$. Because of this difference, the equations we give here are only accurate to leading order in v/c , rather than to first order. In practice, this should make little difference in the outcome, since $v/c \ll 1$ everywhere in our calculation. We discuss the applicability of our equations, including the limitations imposed by the approximations we adopt, in § 4.1.

2.2. Models for Dust and Protostars

To complete our specification of the problem, we must adopt models to describe the dust, the primary source of opacity, and protostellar evolution. We approximate that the dust and gas are well coupled and neglect the possibility that the grain population evolves with time or with position except as a function of local gas properties. We also assume that dust grains react quickly to changes in temperature, so that changes in opacity due to changes in the grain population (such as sublimation of certain grain components) occur without any time delay. This enables us to specify the Planck- and Rosseland-mean opacities as simple functions

of the radiation temperature. We adopt the dust model of Pollack et al. (1994), which includes six species of dust grains, each with its own sublimation temperature. We approximate the tabulated opacities computed by Pollack et al. using a simple piecewise-linear analytic formula. Our fit gives

$$\kappa_P = \begin{cases} 0.3 + 7.0(T_r/375), & T_r \leq 375, \\ 7.3 + 0.7(T_r - 375)/200, & 375 < T_r \leq 575, \\ 3.0 + 0.1(T_r - 575)/100, & 575 < T_r \leq 675, \\ 2.8 + 0.3(T_r - 675)/285, & 675 < T_r \leq 960, \\ 3.1 - 3.0(T_r - 960)/140, & 960 < T_r \leq 1100, \\ 0.1, & T_r > 1100, \end{cases} \quad (10)$$

$$\kappa_R = \begin{cases} 0.1 + 4.4(T_r/350), & T_r \leq 350, \\ 3.9, & 350 < T_r \leq 600, \\ 0.7, & 600 < T_r \leq 700, \\ 0.25, & 700 < T_r \leq 950, \\ 0.25 - 0.15(T_r - 950)/50, & 950 < T_r \leq 1000, \\ 0.1, & T_r > 1000, \end{cases} \quad (11)$$

where the radiation temperature T_r is in kelvins and κ_P and κ_R are in square centimeters per gram. Note that due to the optical thickness of a massive core, $T_r \approx T_g$ everywhere within one except near its surface. Note also that at high temperatures where the dust has sublimed, our choice to set $\kappa_P = \kappa_R = 0.1 \text{ cm}^2 \text{ g}^{-1}$ is purely a numerical convenience we use to represent a “small” opacity. The true opacity depends in detail on the radiation spectrum and the physical state of the gas (molecular, atomic, or ionized), but is certainly much smaller than the opacity due to dust grains. However, sharp opacity gradients make it difficult for our radiation iterative solver to converge, so the choice of $0.1 \text{ cm}^2 \text{ g}^{-1}$ is a compromise between physical realism and numerical efficiency. This choice has little effect in practice, because for the simulations we describe here only a handful of computational cells reach temperatures high enough to be in this regime.

The final piece of our physical model is a method for specifying the luminosity of accreting protostars, which appears as a source term in the radiation energy equation. The input to this model is the mass accretion history of the protostar, which is determined with the sink particle algorithm of Krumholz et al. (2004), which we discuss in more detail in § 2.3. We adopt the protostellar evolution model of MT03, an extension of earlier models by Nakano et al. (1995, 2000). The model is fairly complex, so we refer readers to MT03 for a detailed description, but we summarize its central features here. The model describes a star as a polytropic sphere and computes the evolution of the protostellar radius, central temperature, luminosity, and polytropic index using the equation of conservation of energy for the star, including terms that describe the energy used to dissociate and ionize the incoming gas and the energy released by deuterium and hydrogen burning. The model includes approximate treatments of the onset of deuterium burning in the core, the exhaustion of deuterium in the core, the formation of a radiative barrier and the formation to a convective envelope, and the start of hydrogen burning. It reproduces the detailed numerical simulations of Stahler (1988) and Palla & Stahler (1992) to $\sim 10\%$. Figure 1 shows a sample calculation using our numerical implementation of the model for the case of a protostar accreting at a constant rate of $10^{-3} M_\odot \text{ yr}^{-1}$.

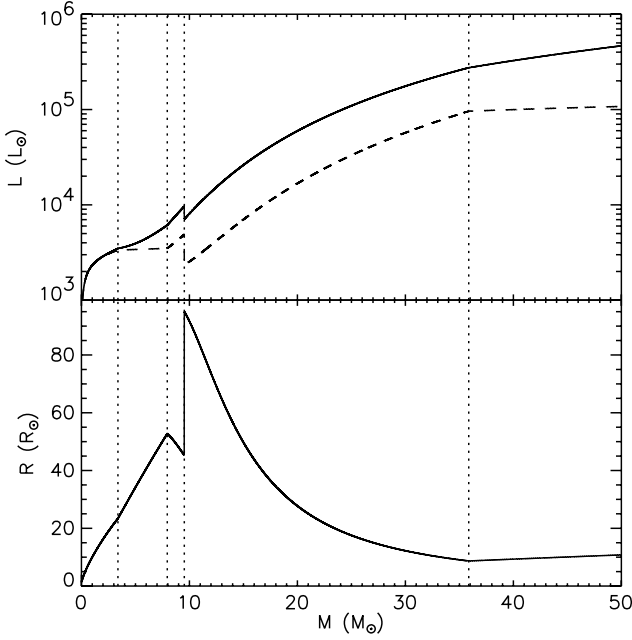


FIG. 1.—Luminosity (*top*) and radius (*bottom*) of a protostar vs. mass computed using our protostellar model with a constant accretion rate of $10^{-3} M_{\odot} \text{ yr}^{-1}$. The dashed line in the top panel is the luminosity due to accretion. The dotted vertical lines mark, from left to right, the masses at which deuterium burning starts, deuterium in the core is exhausted, convection in the envelope starts, and hydrogen burning starts.

2.3. Solution Algorithm

We solve the evolution equations using the Orion adaptive mesh refinement (AMR) code. The code consists of three primary modules, which operate sequentially in each update cycle.

First is the hydrodynamics module (Puckett & Saltzman 1992; Truelove et al. 1998; Klein 1999), which solves the Euler equations of gas dynamics (eqs. [1], [2], and [3]), including all of the terms except those involving radiation. The hydrodynamics module uses a conservative Godunov scheme with an approximate optimized Riemann solver (Toro 1997). The algorithm is second-order accurate in time and space for smooth flows and provides a robust treatment of shocks and discontinuities using very little artificial viscosity.

The second part of the code is the gravity module, which computes the gravitational potential from the Poisson equation (eq. [6]) using a multigrid iteration scheme (Truelove et al. 1998; Klein 1999; Fisher 2002).

The third part is a radiation module, which is updated using the Krumholz et al. (2007) operator splitting approach, in which we update the dominant radiation terms describing diffusion and emission minus absorption implicitly using the approach of Howell & Greenough (2003) while we update the work and advection terms explicitly. This algorithm is stable and accurate for problems in the static diffusion limit such as ours, and we refer readers to Howell & Greenough (2003) and Krumholz et al. (2007) for a detailed discussion of the algorithm and the tests we have performed with it. For the radiation update, we use the dust model described in § 2.2 to compute the opacities, and we use the luminosity of each protostar, computed as described below, as a source term.

We supplement these modules by using the Eulerian sink particle algorithm of Krumholz et al. (2004) to handle the formation of protostars. When a cell on the finest AMR level violates the Jeans condition for gravitational stability (Truelove et al. 1997),

we create a “star particle” in that cell. Each such particle is a sink particle, as described by Krumholz et al. (2004), but also has a corresponding protostellar model, which in addition to the mass includes the star’s radius, luminosity, polytropic index, accretion rate, mass of deuterium remaining, and phase of evolution (e.g., whether the star has developed a convective envelope yet). In each update cycle, after completing the standard update step for sink particles, we also update the protostellar model. When we perform a radiation update, the protostellar luminosity becomes a source term in the radiation energy equation.

All of these pieces operate with the AMR framework (Berger & Oliger 1984; Berger & Collela 1989; Bell et al. 1994). We cover the computational domain with a series of levels $l = 0, 1, 2, \dots, L$, where $l = 0$ is the coarsest level, which covers the entire computational domain. Each level is a union of rectangular grids, which need not be contiguous. The grids are nested, such that every grid on level $l > 0$ is entirely enclosed within one or more grids on level $l - 1$. Grids on a given level all have the same grid spacing Δx^l , and spacings on different levels are related by integer ratios $f > 1$, so that $\Delta x^{l+1} = \Delta x^l / f$. For all the calculations we present here, we use $f = 2$. Each level advances with its own time step Δt^l , and time steps on adjacent levels obey the relation $\Delta t^{l+1} = \Delta t^l / f$. The process for advancing the calculation is recursive. To advance a time step on level l , one first updates all the level l cells through a time Δt^l , then updates all the cells on level $l + 1$ through f time steps of size Δt^{l+1} . However, after completing each level $l + 1$ update, one advances the cells on level $l + 2$ through f time steps, and so forth down to the finest level present. After every f cycles on each level $l > 0$, we perform a synchronization procedure between levels l and $l - 1$ to ensure that mass, momentum, and energy are conserved across level boundaries.

The overall time step is set by the Courant condition computed on each level,

$$\Delta t^l = C \frac{\Delta x^l}{\max(|v| + c_{\text{eff}})}, \quad (12)$$

where the maximum is taken over all cells on that level. The effective sound speed is

$$c_{\text{eff}} = \sqrt{\frac{\gamma P + (4/9)E(1 - e^{-\kappa_R \rho \Delta x})}{\rho}}, \quad (13)$$

where γ is the ratio of specific heats for the gas, and the factor $(1 - e^{-\kappa_R \rho \Delta x})$ provides a means of interpolating between optically thick cells, where radiation pressure contributes to the restoring force and thus increases the effective signal speed, and optically thin cells, where radiation does not provide any pressure. To enforce the integer ratio between time steps on different levels, after computing the time step Δt^l on each level, we set the time step on level 0 to $\Delta t^0 = \min(\Delta t^l f^l)$, then reset the time step on all other levels to $\Delta t^0 / f^l$.

2.4. Initial, Boundary, and Refinement Conditions

We choose initial conditions that correspond to the analytic model of MT03 for high-mass cores. Each calculation begins with an initial core that is a sphere of gas of mass M and radius r_1 . The core is centrally concentrated, with density profile $\rho \propto r^{-3/2}$, down to some inner radius r_0 . Inside r_0 the density is constant. This corresponds approximately to the thermally supported core and turbulently supported envelope of a MT03 core. To impose the initial turbulent velocity field, we generate a 1024^3 grid of

TABLE 1
SIMULATION PARAMETERS

Run Name (1)	Mass (M_{\odot}) (2)	Field (3)	EOS (4)	r_1 (pc) (5)	r_0 (AU) (6)	L (pc) (7)	$\Delta x^{l_{\max}}$ (AU) (8)	ρ_1 ($10^{-14} \text{ g cm}^{-3}$) (9)	t_{ff} (kyr) (10)	σ (km s^{-1}) (11)
100A.....	100	A	RT	0.1	38.4	0.6	7.5	1.0	52.5	1.7
100B.....	100	B	RT	0.1	38.4	0.6	7.5	1.0	52.5	1.7
200A.....	200	A	RT	0.14	53.5	0.85	10.7	0.72	62.4	2.0
100ISO.....	100	A	ISO	0.1	38.4	0.6	7.5	1.0	52.5	1.7

NOTES.—Col. (3): Perturbation field, A or B. Col. (4): Equation of state; RT = radiative transfer, ISO = isothermal. Col. (7): Grid spacing on finest AMR level. Col. (8): Initial density of inner, constant-density region. Col. (9): Free-fall time at the mean density.

perturbations with a power spectrum $P(k) \propto k^{-2}$ using the method of Dubinski et al. (1995) corresponding to the spectrum expected for supersonic shock-dominated turbulence. We overlay the perturbation cube on the core such that the core just fits inside the perturbation cube and assign the velocity at every point in the cube to the corresponding point inside the core. The use of a 1024^3 grid allows turbulent power to be present down to scales of $1/1024$ of a cloud diameter, which is approximately the diameter of the nonturbulent, thermally supported region in the MT03 model. We scale the total velocity of the core so that the one-dimensional core velocity dispersion is $\sigma = (GM/r_1)^{1/2}$, the dispersion required for the core to be in approximate hydrostatic balance. We do not drive the turbulence or otherwise inject energy after the simulation starts. We set the initial temperature of the core to $T_g = 20$ K and the initial radiation energy density to $1.21 \times 10^{-9} \text{ ergs cm}^{-3}$, the energy density of a blackbody radiation field at $T_r = 20$ K temperature.

Outside the core is an ambient medium with density 100 times smaller than the density at the edge of the core and temperature 100 times higher, so the core and ambient medium are in thermal pressure balance. The opacity of the ambient medium is set to zero, so that it cannot cool, radiatively heat the core, or inhibit the escape of radiation from the core.

We place the core and ambient medium inside a computational cube centered on the origin with length L , chosen large enough so that no core material ever approaches the edge of the computational domain. At the boundary we impose symmetry conditions on the hydrodynamic evolution, Dirichlet conditions for the gravitational field, with the potential on the boundary set equal to $-GM/r$, and Marshak boundary conditions on the radiation field. Marshak conditions are a variant of Neumann conditions in which the flux into the computational domain is set to a constant value of $cE_0/2$, where we set E_0 equal to the initial radiation energy density. The flux out of the computational domain at the face of each cell on the boundary is set equal to $cE/2$, where E is the radiation energy density in the cell. This condition imposes a uniform 20 K radiation bath, but allows excess radiation generated inside the computational domain to escape freely.

The final piece of our computational setup is the refinement conditions, which determine when new high-resolution grids are created or when existing ones are removed, a process that occurs automatically throughout the calculation. We use three refinement criteria. First, in order to prevent numerical fragmentation we refine any cell on level l in which the density of that cell violates the Jeans condition for self-gravitational stability (Truelove et al. 1997),

$$\rho < \rho_J = J^2 \frac{\pi c_s^2}{G(\Delta x^l)^2}. \quad (14)$$

We use a Jeans number $J = 1/8$. Second, we refine any cell whose distance from the nearest sink particle is less than $16\Delta x^l$, so that the region around sink particles is always well-resolved. Third, to ensure that we do not produce artificially large radiation pressure forces due to poorly resolved radiation energy density gradients, we refine any cell in which $\Delta x^l |\nabla E|/E > 0.25$, i.e., anywhere the radiation energy density changes by more than 25% per cell. All of these refinement criteria are applied up to a maximum level L_{\max} , which we specify when we begin the calculation. All runs use a resolution of 128^3 cells on level 0 and a maximum level of 7, giving an effective resolution of $16,384^3$.

We perform four runs, whose properties we summarize in Table 1. Run 100A is our baseline run to which we compare the others. We show the initial density and velocity field for this run in Figure 2. Run 100B uses the same parameters as run 100A and has a turbulent velocity field with the same power spectrum, but a different random realization than run 100A. This allows us to study how the random velocity field influences the results. Run 200A uses the same velocity field as 100A, but a more massive core, enabling us to study how our results depend on initial core mass. We keep the mean column density constant, so that we are not changing the average opacity to radiation. Finally, run 100ISO uses the same initial conditions as run 100A, but for it we do not use radiative transfer. Instead, we use an isothermal equation of state fixed to $T_g = 20$ K. This amounts to setting $E = 0$ and $B = 0$ in equations (2) and (3) and dropping equation (4) entirely. This lets us isolate how radiative transfer affects the results and

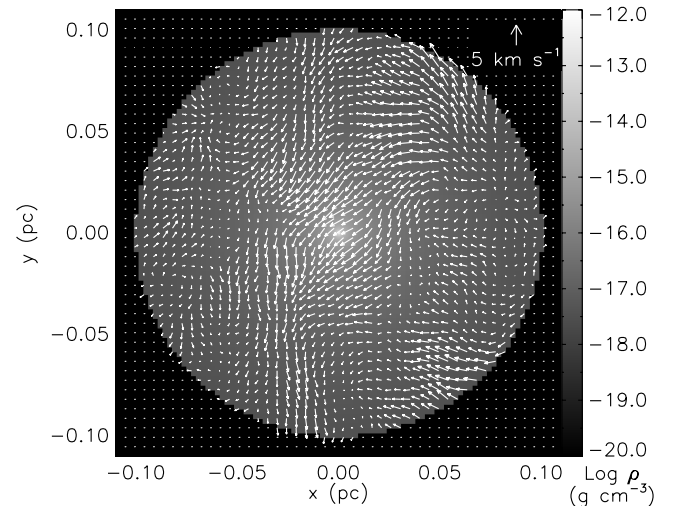


FIG. 2.—Slice through the (x, y) -plane showing the density (gray scale) and velocity (arrows) fields at the start of run 100A. [See the electronic edition of the Journal for a color version of this figure.]

study whether simulations that do not include it are reliable. Run 100ISO is very similar in setup to some of the models evaluated by Dobbs et al. (2005).

3. RESULTS

We evolve each run for 20 kyr, which is 38% of a mean-density free-fall time for runs 100A, 100B, and 100ISO and 32% of a mean-density free-fall time for run 200A. For the radiative runs, in all cases the most massive star formed by the end of the run has begun deuterium burning and thus should rise rapidly in luminosity thereafter (see Figure 1), strongly inhibiting further fragmentation. The portion of the evolution we follow therefore includes the primary fragmentation phase, during which the densest parts of the core collapse and the pattern of fragmentation is established. As we discuss in § 3.4.2, there may be subsequent secondary fragmentation in unstable protostellar disks at later times, but this does not significantly change where most of the collapsing mass goes.

In the analysis that follows, we consider sink particles stars only if they have a mass of $0.05 M_{\odot}$ or more, the mass at which “second collapse” to protostellar densities occurs (Masunaga et al. 1998; Masunaga & Inutsuka 2000). (Smaller mass objects can still collapse to form stars or brown dwarfs, but they produce insufficient pressure to produce rapid dissociation of molecular hydrogen, leading to second collapse. Instead, they contract much more slowly.) We take this precaution because a few times over the course of a run our radiation implicit solver fails to converge and produces an unrealistically low temperature in an isolated cell. The low-temperature cell may be Jeans unstable and form a sink particle (see Krumholz et al. [2004] for a discussion of the sink particle creation algorithm). These artificially created sink particles are harmless because they contain negligible mass, at most a few times $10^{-2} M_{\odot}$, usually much smaller. Since the radiation solver generally recovers on the next time step and produces a reasonable temperature and the regions around the sink particles are gravitationally stable once a normal temperature is restored, these low-mass sink particles do not accrete or radiate at a noticeable rate and never contain a significant amount of mass. We impose a mass threshold before we consider a sink particle to be a protostar in order to eliminate these spurious objects. This condition may cause us to mischaracterize some real, nonnumerical but very low mass stars, but the amount of mass in stars we could miss in this fashion is obviously tiny. Although the isothermal run is clearly not subject to this problem, we impose the same condition on our analysis of it to avoid introducing any bias.

Each of the radiative runs required roughly 60,000–70,000 CPU hours on an IBM SP, running in parallel on 128 processors. The isothermal run required approximately 10,000 CPU hours.

3.1. Summary of Evolution

We summarize the evolution of our runs starting with run 100A, and we then discuss how the other runs differ. We defer discussion of how fragmentation and protostar formation occurs across the runs until § 3.2 and here focus on the overall qualitative morphology of the gas.

3.1.1. Run 100A

Figure 3 shows a time sequence of the evolution of the run, starting from the initial state shown in the top row. Turbulent motions delay the onset of collapse for a while, but as the turbulence decays gas starts to collapse. The first object, which we refer to hereafter as the primary star, appears 5.3 kyr after the start of the simulation. It forms in a shocked filament, which continues

to accrete mass and by 6 kyr is beginning to form a flattened protostellar disk. The second row shows the state of the simulation at this point.

As the evolution continues, several more dense condensations appear, but most of these are unable to collapse and form a protostar before reaching the primary star and being sheared apart in the protostellar disk. At 12.2 kyr a second protostar forms, but it falls into the primary star and merges with it at 12.7 kyr, before it has accreted $0.1 M_{\odot}$ of gas. At the time of merging the primary star is already $2.1 M_{\odot}$, so the mass gained in the merger is negligible. The third row shows the state of the simulation at 12.5 kyr, about halfway between when the second star appears and when it merges with the primary. We should at this point mention a caveat regarding resolution. Because of our limited resolution, we are unable to resolve binaries in orbits closer than 8 cells, or 60 AU. This means that it is likely that at least some of the mergers identified by our code are really formations of tight binaries. We discuss the implications of this in greater detail in our discussion of numerical resolution issues in § 4.2. Here, we simply mention that whether the true outcome is a merger of a tight binary probably makes very little difference to the overall evolution, since the smaller star carries negligible mass compared to the primary.

Only after 14.4 kyr does one of the condensations collapse to form a second protostar that is not immediately accreted, as shown in the fourth row of Figure 3. At this point the primary star is $3.2 M_{\odot}$ and has a well-defined massive disk. The condensation from which the new protostar forms is already visible in the third row. It is able to collapse and form a protostar, unlike several others, because it is fairly distant from the central object. This reduces the amount of radiative heating to which it is subjected, a topic we discuss in more detail in § 3.3.

The next significant change in the system occurs when one of the arms of the disk becomes unstable and fragments to form a third protostar at 17.4 kyr. We show the configuration just after this in the fifth row. At this point the central star mass is $4.3 M_{\odot}$. The disk mass cannot be defined precisely, because the disk does not have a clearly defined edge. However, we can get an approximate mass by defining the disk as all the cells within 1000 AU of the primary star denser than $10^{-15} \text{ g cm}^{-3}$. This gives a mass range of $3.1 M_{\odot}$. We discuss our definition for the disk edge, and disk fragmentation in general, in § 3.4. The fragment is very small compared to the central protostar, and remains so as the simulation continues to evolve.

The configuration after 20 kyr of evolution, shown in the sixth row of Figure 3, is substantially similar. Two more small disk fragments form, but they both collide with the primary star almost immediately after formation, when their masses are $<0.1 M_{\odot}$. This has a negligible effect on the mass of the primary. At the end of 20 kyr, the primary star is $5.4 M_{\odot}$, the second star is $0.34 M_{\odot}$, and the third star, which formed in the disk of the first, is $0.20 M_{\odot}$. The disk itself is $3.4 M_{\odot}$ in mass. Thus, the system is well on its way to forming a massive star, and thus far the vast majority of the collapsed mass has concentrated into a single object. We show a larger plot of the full core at this point in Figure 4.

We show the evolution of the primary star’s radius, mass accretion rate, and luminosity in Figure 5. The model of MT03 gives an accretion rate onto the star-disk system of $1.2 \times 10^{-4} (m_{*d}/1 M_{\odot})^{1/2} M_{\odot} \text{ yr}^{-1}$, where m_{*d} is the mass of the star plus the disk. If we assume that the accretion rate onto the star is a fraction m_{*}/m_{*d} of this, we infer an accretion rate of about $2 \times 10^{-4} M_{\odot} \text{ yr}^{-1}$ onto the star, which is comparable to the simulation result at the end of the calculation; at earlier times, the simulation gives a higher accretion rate. There are at least three reasons for this. First, we assume that the density in the central

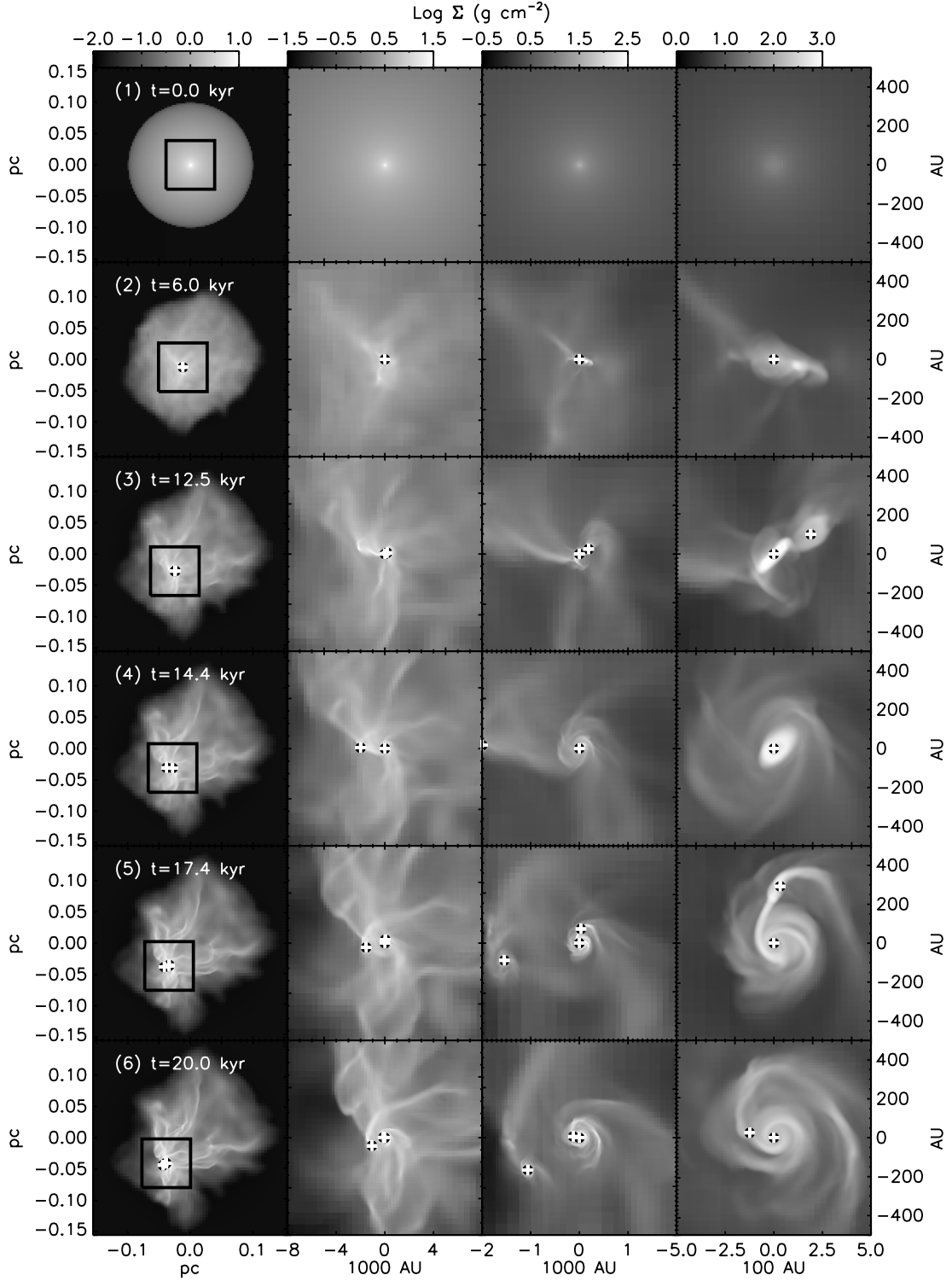


FIG. 3.—Column density as a function of time in run 100A. From top to bottom, the rows show the cloud state at increasing time, as indicated. From left to right, each step to the right corresponds to decreasing the linear size of the region displayed by a factor of 4, from a 0.31 pc region in the left column to a 1000 AU region in the right column. At the top of each column we give a scale bar for the images in that column. In the left column the region shown is always centered on the origin, and the region shown in the second column is indicated by the black box; in the other columns, the region shown is centered on the location of the primary star at that time. Stars are indicated by the white plus signs. All images are shown in the same projection. [See the electronic edition of the *Journal* for a color version of this figure and an mpeg animation.]

regions was initially constant, whereas MT03 assume that the power-law increase in density continues all the way to the origin; as a result, accretion is delayed for 6 kyr in the simulation, whereas it begins immediately in the analytic model, thereby spreading the accretion over a longer time. Second, MT03 as-

sume that the turbulence is undamped, whereas it is damped in somewhat less than a crossing time in the simulation, which increases the accretion rate. Third, our primary star forms out of a single large, shocked filament, and accretion onto it is dominated by gas from this filament. The shock raises the density and thereby

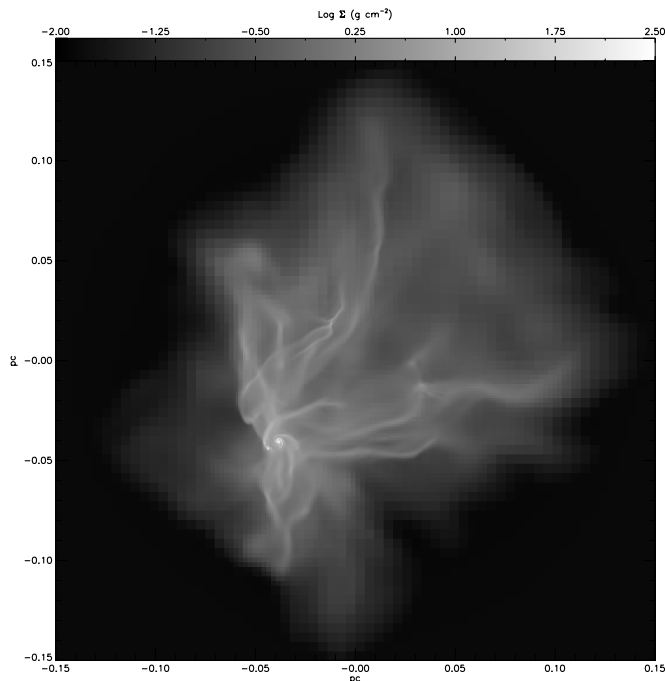


FIG. 4.—Column density at 20 kyr in run 100A. We do not show the positions of stars. [See the electronic edition of the *Journal* for a color version of this figure.]

enhances the accretion rate relative to what the MT03 model predicts.

3.1.2. Run 100B

Run 100B uses the same parameters as run 100A, but a different random realization of the initial turbulent velocity field. The evolution in detail is of course different from run 100A, but qualitatively it is quite similar. Figure 6 shows a time sequence of column densities at the same times as in run 100A. On the largest scales, as in run 100A, at late times the core is dominated by large-scale filaments. There is a primary star at the center of this filament network, and on smaller scales it is surrounded by a disk. The disk is somewhat denser and less extended than in run 100A, but differs in size by less than a factor of 2.

In run 100B, a primary star forms at 5.4 kyr, and a second object forms at 7.8 kyr. However, the two merge at 9 kyr, when the primary is $2.0 M_{\odot}$ and the secondary is only $0.17 M_{\odot}$. By 12.5 kyr, as Figure 6 shows, the primary is surrounded by a well-defined flattened disk. Accretion onto the primary slows down after that point, and the disk around it remains fairly stable until the primary collides with a second star at 16.1 kyr. This increases the primary's mass from 4.2 to $5.1 M_{\odot}$, and the accretion rate increases thereafter, since the collision brings in an amount of gas considerably larger than the amount of mass the primary gains by the collision itself. This also reduces the angular momentum in the disk around the primary, allowing more gas to accrete and the disk to become more compact. As a result of these two effects, the primary grows from 5.1 to $8.9 M_{\odot}$ in the 4 kyr after the collision, gaining roughly 3 times as much mass from gas accretion as from the collision.

The disk around the primary looks similar to that in run 100A at times before the collision at 16.1 kyr, including the beginnings of spiral structure. However, after the collision the disk is denser and more compact and lower in mass relative to the star. At 20 kyr the disk mass is $2.4 M_{\odot}$, roughly a quarter of the mass of the star. Because of its smaller mass and radius, the disk appears to be more stable than the disk in run 100A, and there is no evidence for disk fragmentation. Since this is a result of the collision, an event that

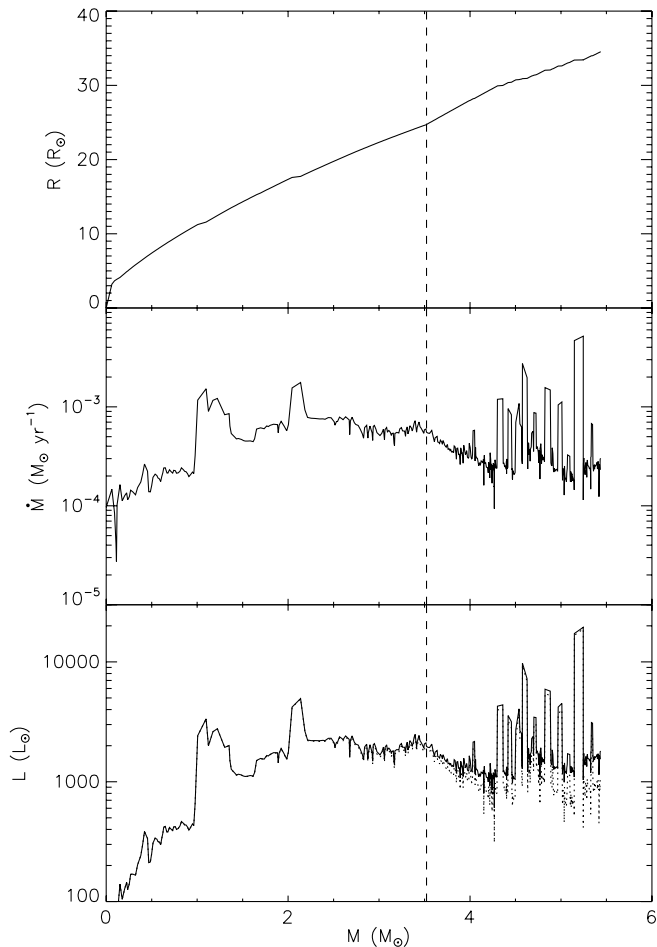


FIG. 5.—Radius, accretion rate, and luminosity of the primary star vs. mass in run 100A. The dashed vertical line indicates the mass at which the star begins burning deuterium. In the luminosity plot the solid line is total luminosity, and the dotted line is the luminosity due to accretion. The two are identical before deuterium burning begins.

shows no signs of being repeated, it seems likely that further evolution will cause the disk to become larger again and return it to a state of instability similar to that of the disk in run 100A.

3.1.3. Run 200A

In run 200A we use the same turbulent velocity field as in run 100A, but impose a $200 M_{\odot}$ core with the same initial column density as the $100 M_{\odot}$ core in run 100A. Figure 7 shows the time sequence of column densities in run 200A at the same times as in run 100A. The overall appearance of the core is very similar to that in run 100A, as are the positions and times of formation of the protostars. This is not surprising given the identical initial velocity fields. A primary star forms at 5.3 kyr, and a second at 11.5 kyr, but this second one merges with the primary at 15.1 kyr. At 16.1 kyr a second fragment forms at a larger distance from the primary, and it survives. In the final time step another pair of small stars forms near the primary. From ~ 10 kyr of evolution onward, the primary has a disk extending several hundred AU out.

At the end of the run, the primary star has reached $8.6 M_{\odot}$, and the accretion disk around it is roughly $6 M_{\odot}$. As in run 100A, there is obvious spiral structure in the disk. Unlike run 100A, there is no disk fragmentation, although in the final time slice one sees a dense condensation that is analogous to the one that formed a protostar out of the disk in run 100A, and this looks likely to produce a fragment. The accretion rate onto the star is roughly

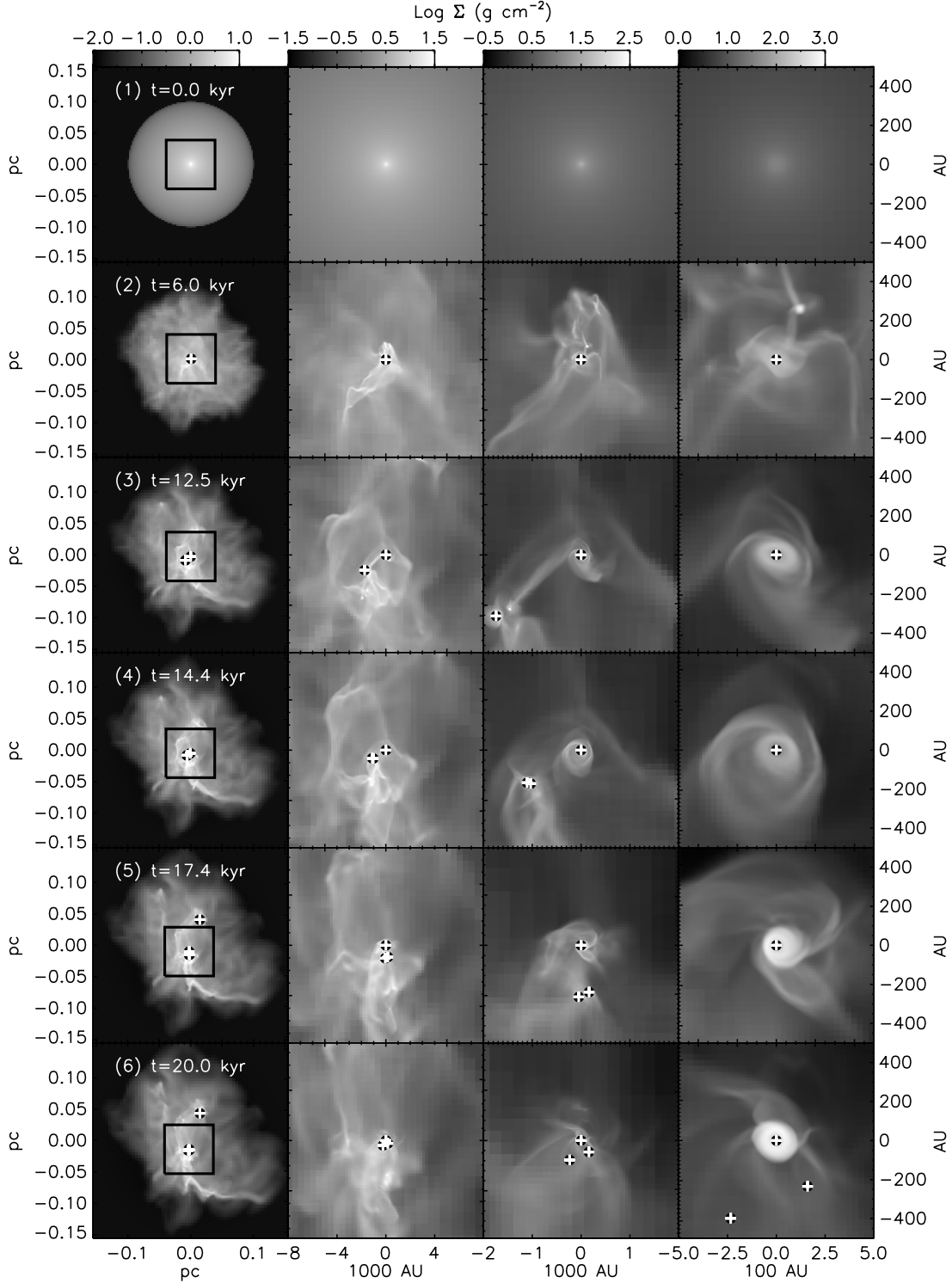


FIG. 6.—Same as Fig. 3, but for run 100B. [See the electronic edition of the Journal for a color version of this figure.]

$5 \times 10^{-4} M_{\odot} \text{ yr}^{-1}$. This agrees well with the MT03 model, which, for the initial conditions in run 200A, predicts an accretion rate of $6.5 \times 10^{-4} M_{\odot} \text{ yr}^{-1}$ onto a $14.6 M_{\odot}$ star-disk system.

3.1.4. Run 100ISO

We show a time sequence for the evolution of the isothermal run at the same times as for run 100A in Figure 8. The overall morphology of the gas is fairly similar on large scales, which is not surprising given the identical initial conditions. A first con-

densation forms, and 2 kyr after the start of the run a primary object forms; it remains the most massive star throughout the run. However, smaller scale runs 100A and 100ISO show very significant differences. Because of its lack of thermal support compared to run 100A, the gas in the isothermal run is much more filamentary. Disks are flatter, filaments have smaller radii, and shock structures are thinner. This causes the evolution to proceed quite differently, so by 20 kyr it is fairly difficult to line up the features from the two runs except at the grossest level of

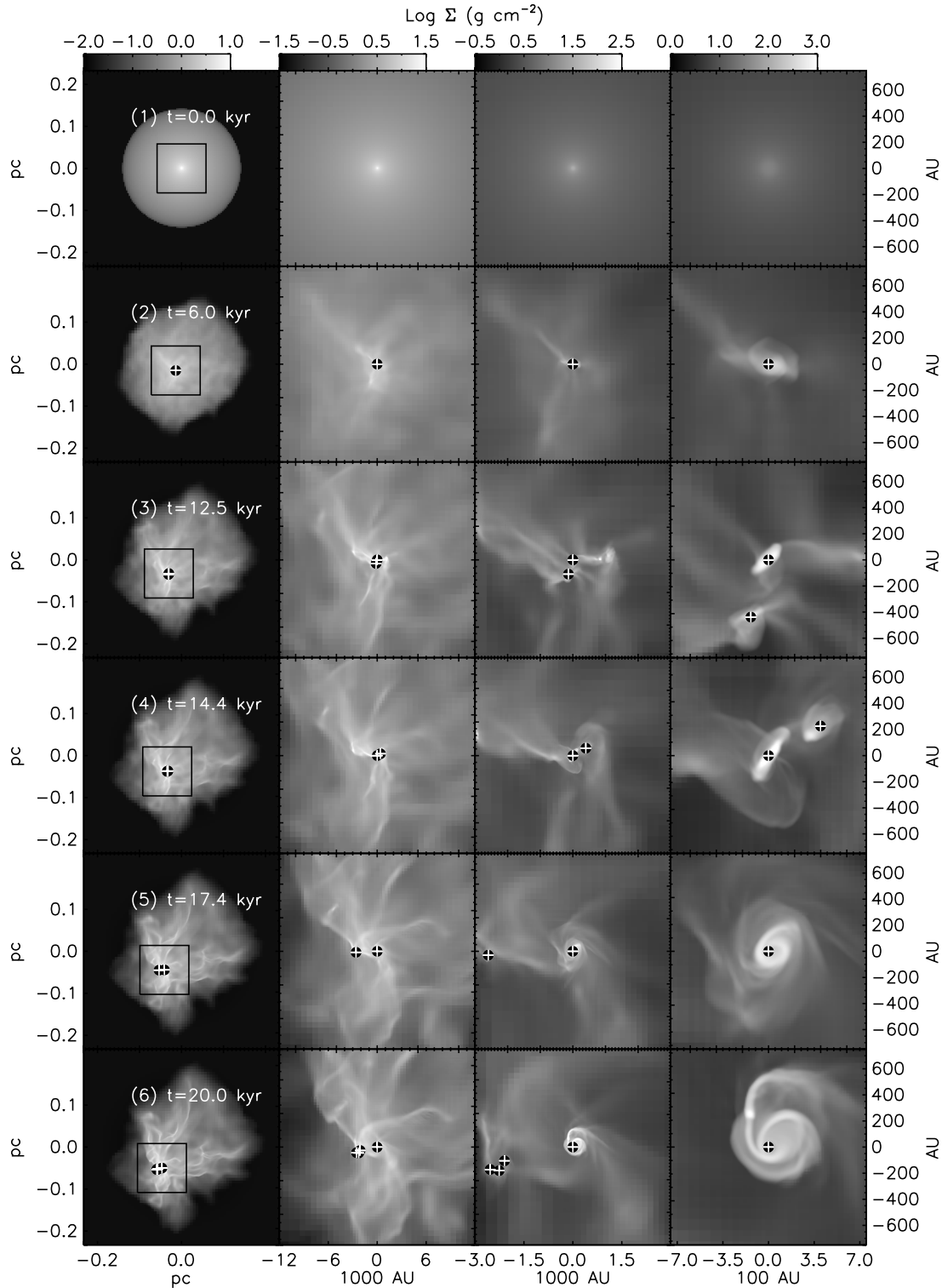


FIG. 7.—Same as Fig. 3, but for run 200A. Note that to accommodate the somewhat larger size of the core, the areas shown in each panel are a factor of 1.5 larger in linear dimension than the analogous panels in Fig. 3. [See the electronic edition of the *Journal* for a color version of this figure.]

the location of protostellar disks and major filaments. There are many more fragmentation sites, and objects are generally much clumpier than in the radiative run. The number of protostars is considerably larger.

3.2. Statistics of Fragment Formation

We summarize the statistics of the stars that form in our simulations in Table 2. In addition to describing the total number and

mass of stars present at the end of the run, we give the total number of stars formed, the total number of significant stellar mergers, defined as those that alter the mass of the more massive merger companion by at least 5%, the final mass of the primary and of all the other stars combined, and the fraction of the primary's mass acquired by mergers rather than accretion, defined as the total mass of all stars that merge with the primary immediately before the merger, divided by the primary's final mass. We show the

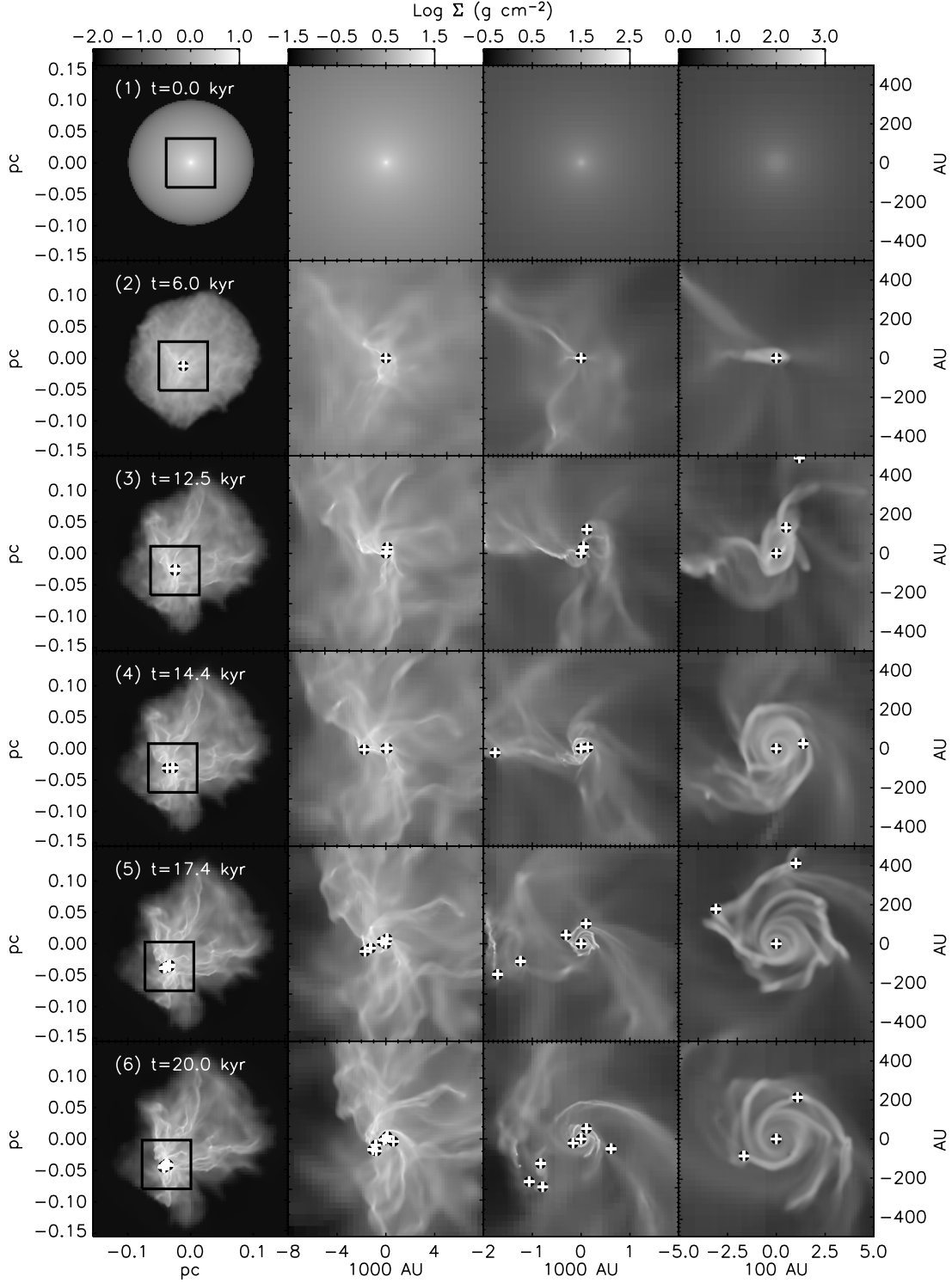


Fig. 8.—Same as Fig. 3, but for run 100ISO. [See the electronic edition of the Journal for a color version of this figure.]

evolution of the mass of the most massive and second most massive stars in all the runs in Figure 9.

The statistics and plot make clear that in all the radiative runs the primary gains mass almost exclusively by accretion. The number of fragments formed is small, and the number surviving at the end of the run even smaller. Moreover, these fragments always contain an extremely small fraction of the total collapsed mass. In none of the radiative runs does the primary star gain more than $\sim 10\%$ of its mass by collisions. There are kinks in the mass versus

time curves shown in Figure 9, indicating sharp rises in the accretion rate, but most of these are due to the primary encountering and accreting dense gas condensations that had not formed stars, not due to mergers. In summary, fragmentation appears to be very weak in massive protostellar cores once we take into account radiative feedback, and stars appear to gain mass by accretion rather than by collisions.

The fragmentation history is very different in run 100ISO. At 20 kyr there are seven protostars in run 100ISO, as opposed to

TABLE 2
STATISTICS OF STARS FORMED

Run (1)	N_{20} (2)	N_{formed} (3)	N_{merge} (4)	M_1 (M_\odot) (5)	M_{other} (M_\odot) (6)	f_{merge} (7)
100A.....	3	6	0	5.4	0.54	0.04
100B.....	4	7	3	8.9	0.31	0.12
200A.....	4	6	2	8.6	0.54	0.06
100ISO.....	7	23	6	7.4	1.5	0.31

NOTES.—Col. (2): Number of stars present at 20 kyr. Col. (3): Total number of stars formed over the 20 kyr evolution, including those that have merged. Col. (4): Number of significant merger events. Col. (5): Mass of primary star to 20 kyr. Col. (6): Total mass of all stars, but the primary at 20 kyr. Col (7): Fraction of primary's mass acquired by mergers.

three in run 100A. There are several more that we do not list because they are just below the $0.05 M_\odot$ cutoff. In the isothermal run, these are certainly real, since there are no potential problems with an iterative radiation solver. Moreover, a factor of 4 more protostars form over the course of run 100ISO than in run 100A, and the fraction of its mass that the primary gains by merging rather than accretion is nearly an order of magnitude larger. As a result, the plot of primary mass versus time shown in Figure 9 is much spikier. Some of the additional stars form out of the disk around the primary, while others form in separate condensations. In several cases we can identify analogous condensations in the isothermal and radiative runs. In the radiative run, these are too hot to collapse, and instead they reach the primary and are accreted, but in the isothermal run they collapse and form protostars.

The fragmentation we see in run 100ISO is mostly consistent with previous work on fragmentation in isothermal simulations, which generally find a great deal of fragment formation. Dobbs et al. (2005) find that a simulation of a $30 M_\odot$ turbulent core forms ~ 30 fragments over an evolution time slightly longer than ours. They do not find any massive stars forming, but that is likely because our effective resolution is considerably lower than theirs (see § 4.2), so they have fewer mergers and more fragment formation around their central object. Simulations with adaptive SPH codes find that for isothermal equations of state, the amount of fragment formation and the typical fragment mass are both highly resolution dependent (Martel et al. 2006). Runs with radiative transfer are unlikely to suffer from this problem, because radiative heating shuts off fragmentation on small scales. (It is worth noting that we could go to higher resolution in the isothermal run, since it is computationally cheaper by a factor of ~ 6 – 7 than runs with radiative transfer. However, to make the comparison as fair as possible, we use the same resolution in the radiative and non-radiative runs.)

3.3. Radiative Heating and Fragmentation

Clearly there is a significant difference between the radiative transfer runs, none of which show much fragmentation and for which the morphology is relatively smooth, and the isothermal run, in which numerous fragments form out of a strongly filamentary morphology and a significant fraction of the primary's mass is acquired through mergers. This suggests that the effective equation of state, including radiative heating, is playing an important role in determining how fragmentation occurs. Examining the distribution of temperature and Jeans mass,

$$M_J = \rho \lambda_J^3 = \left(\frac{\pi k_B T}{G \mu} \right)^{3/2} \rho^{-1/2}, \quad (15)$$

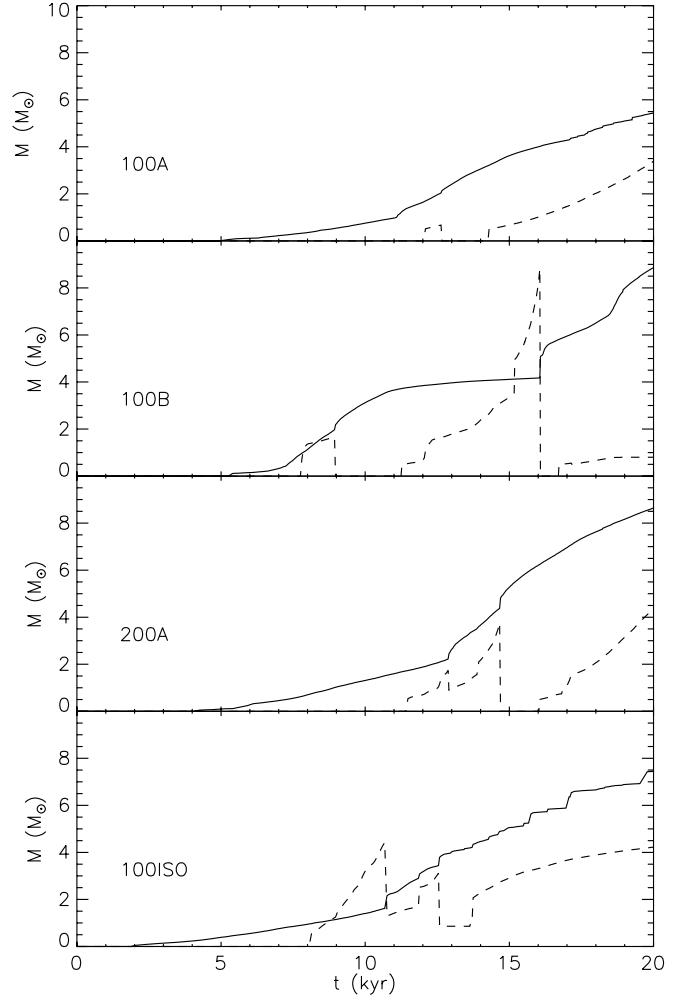


FIG. 9.—Mass of most massive star (solid line) and 10 times the mass of the second most massive star (dashed line) as a function of time in all runs. Sudden increases in mass correspond to points where a smaller star merges with a bigger one. Sudden decreases in mass correspond to the points where the title “second most massive” star suddenly changes from one star to another, because the previous second most massive star has merged with the most massive.

in our simulations supports this hypothesis. For reference, in the initial state the Jeans mass at the core edge is $3.4 M_\odot$, at the mean density it is $2.4 M_\odot$, and at the central density it is $0.03 M_\odot$. Note that this Jeans mass is 4.71 times the Bonnor-Ebert mass, so centrally condensed objects with masses considerably smaller than M_J can still be unstable.

In Figure 10 we plot for run 100A the mass $M(>T)$ of gas with temperature greater than T , at a time shortly after the first fragment other than the primary star forms (12.5 kyr) and at the final time in the run (20 kyr), and in Figure 11 we show the spatial distribution of the gas as a function of temperature at 12.5 kyr. Clearly by the time the second star forms, radiation from the primary has heated a significant fraction of the core to well above its initial temperature. The temperature is above 50 K in $4.4 M_\odot$ of gas, including almost all the gas within 1000 AU of the primary object, which is where much of the fragmentation takes place in our isothermal run and in other isothermal simulations in the literature (e.g., Bate et al. 2003). By 20 kyr the mass heated to more than 50 K is $6.0 M_\odot$, extending more than 2000 AU away from the primary star.

To study how this heating is likely to affect fragmentation, in Figure 12 we show a scatter plot of density versus temperature for the mass in run 100A at 12.5 kyr. From the plot it is clear that

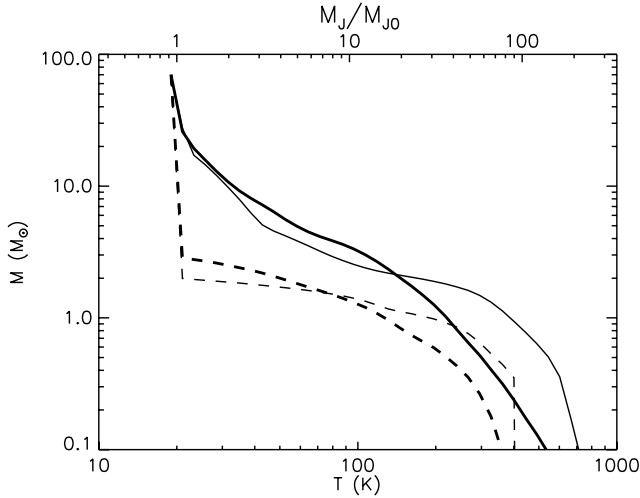


FIG. 10.—Mass of gas above temperature T as a function of T in run 100A. The curves do not reach $100 M_{\odot}$, because this analysis only includes gas with a density more than twice the initial density at the edge of the core, to ensure that there is no confusion with the ambient medium. We show the state of the run at 12.5 kyr, just after the second fragment forms (*thin solid line*), and at the end of the run, 20 kyr (*thick solid line*). We also show the distributions at those times computed using temperatures derived from a barotropic equation of state rather than the true temperatures in our run (*thin and thick dashed lines*). The top axis shows the ratio of Jeans mass M_J at temperature T to Jeans mass M_{J0} in gas of the same density at the initial temperature $T_0 = 20$ K. For gas at the mean density of the initial core, $M_{J0} = 2.4 M_{\odot}$.

almost all of the very dense gas, where fragmentation might take place, is heated to hundreds of kelvins. However, this heating begins at relatively low densities, so almost all the gas denser than 10 times the initial density has been heated at least somewhat. The ρ - T distribution is roughly bounded by $T \propto \rho^{\gamma-1}$

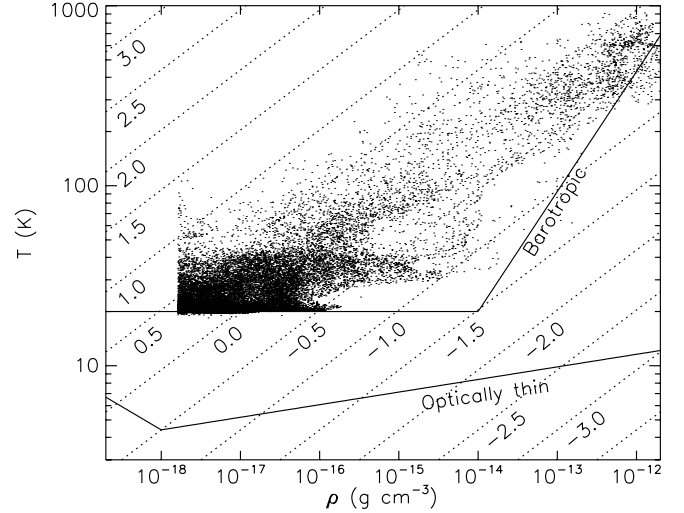


FIG. 12.—Scatter plot showing temperature vs. density for a sample 50,000 cells in run 100A at time 12.5 kyr. Cells are selected with a probability proportional to their mass, so the density of points is a true representation of the mass distribution, with the exception that we exclude cells with densities below twice the initial cloud edge density to ensure that we exclude the ambient medium. The diagonal dotted lines are curves of constant Jeans mass. The number next to each line indicates the value of $\log(M_J/M_{\odot})$ to which it corresponds. The solid lines are the curves of ρ vs. T for the barotropic equation of state of Dobbs et al. (2005) and for the optically thin heating and cooling model of Larson (2005).

with $\gamma = 1.2$ – 1.3 over the full range of the density distribution. The exact shape changes at other times, but the general feature that the temperature rises continuously with density, with no large isothermal density range, persists at all times after the primary object forms.

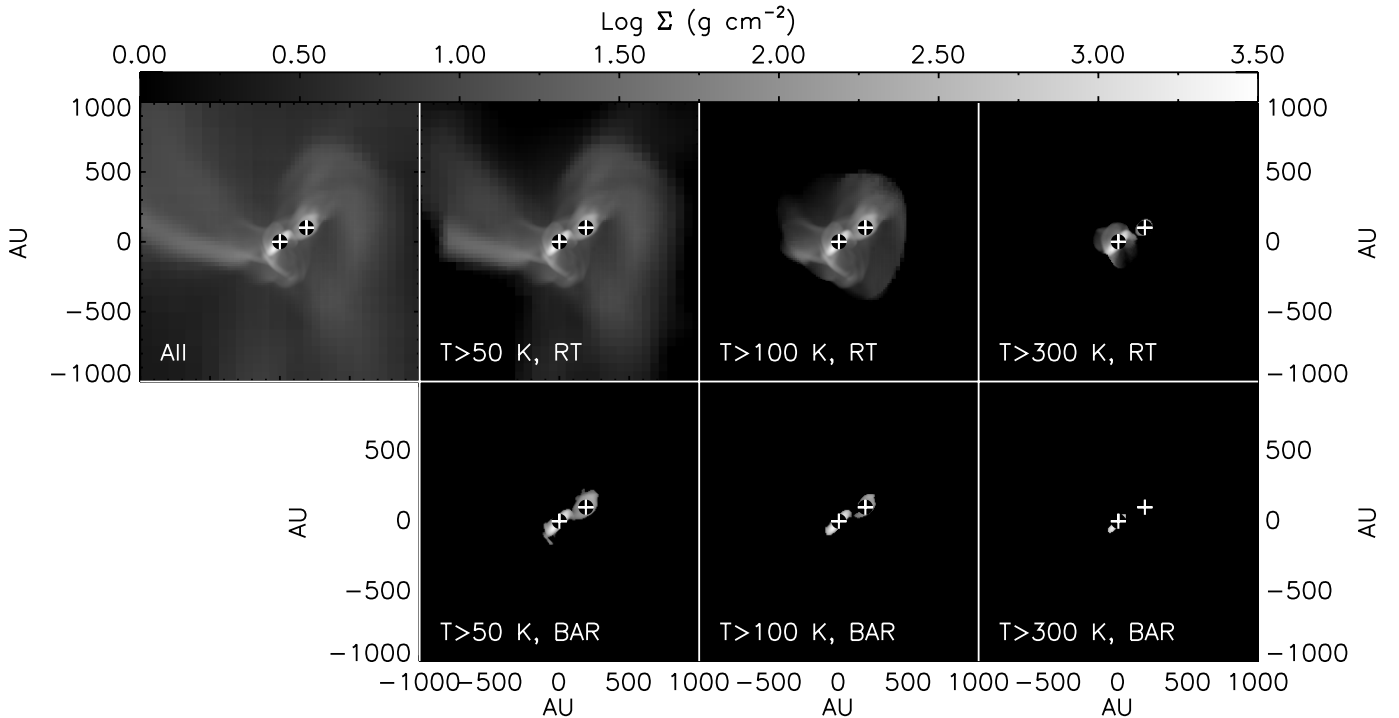


FIG. 11.—Column density in run 100A of gas above the temperature indicated in each panel. The top left panel shows all the gas ($T > 0$), and the top row shows gas above temperatures of 50, 100, and 300 K. The bottom row shows the column density above those temperatures, but using temperatures computed from a barotropic equation of state rather than the actual temperature in the run. Stars are indicated by white plus signs. The time shown is the same one shown in Fig. 3, row 3: 12.5 kyr, shortly after the time the second protostar forms. [See the electronic edition of the Journal for a color version of this figure.]

Since the rise is slower than $T \propto \rho^{1/3}$, the Jeans mass does decline as one moves to higher density material, and so except at the highest densities and temperatures, there is generally more than a thermal Jeans mass of material above any given density. At the mean density and temperature of the core, there are still many thermal Jeans masses. However, the continuous rise of T with ρ in our core still provides an explanation why we see so little fragmentation. Simulations (Li et al. 2003; Jappsen et al. 2005; Bonnell et al. 2006) and analytic work (Larson 2005) suggest that how fragmentation in a turbulent medium proceeds depends critically on the value of γ , with fragmentation proceeding to arbitrarily small masses as long as $\gamma < 1$ and ceasing for $\gamma > 1$. The physical argument behind this result is that in a turbulent medium, the densest structures formed by the turbulence are generally filaments. Gravitationally unstable filaments are able to collapse axisymmetrically toward their centers when $\gamma < 1$, but are unable to collapse axisymmetrically for $\gamma > 1$. If the rate of radiative heating and cooling has a density dependence such that $\gamma < 1$ at low densities and $\gamma > 1$ at high densities, then fragments will form at the density corresponding to the transition between these two, because at this density contraction of filaments along their axes will stall, and the filament will break up into “beads” instead.

Figure 12 shows that in a massive core with an accreting protostar in its center, $\gamma > 1$ effectively over the entire core. There is a region of points with $\gamma \approx 1$, in the form of the line of points at $T \approx 30$ K at densities from 10^{-16} to 10^{-14} g cm $^{-3}$, and indeed these points do represent the gas from which the next fragment forms, at 14.4 kyr of evolution. They are relatively cool, because they are ~ 3000 AU from the primary star and are sufficiently dense to be self-shielding against its radiation. However, these points are the exception, and overall, such self-shielding distant structures form only rarely. This is likely why we see so little fragmentation despite the fact that our simulation contains many tens of thermal Jeans masses. Filaments do form, but they are unable to even begin contracting because radiative heating keeps them at $\gamma > 1$. Rather than contracting, stalling, and breaking up into beads, they never begin contracting in the first place, and instead their mass drains onto the primary star or its disk.

It is important to note that the energy source in our simulation responsible for raising the temperature is almost entirely accretion onto the primary star. At 12.5 kyr the primary star has not yet started burning deuterium and is only $2 M_{\odot}$, so the luminosity all comes from accretion. At 20 kyr deuterium has ignited but is only generating $\sim 50\%$ of the total luminosity. Thus, the heating does not depend on nuclear burning in the primary star. Accretion luminosity by itself is sufficient to greatly reduce fragmentation. However, as the luminosity rises due to nuclear burning, the effect should become even more significant.

For comparison, in Figures 10 and 11 we also show results using the density distribution in our simulation, but using temperatures computed from a barotropic equation of state rather than the real temperatures in the simulation. Simulations have used a variety of barotropic equations of state. We compare to one from Dobbs et al. (2005), which generally produces higher temperatures than those used elsewhere (e.g., by Bate et al. 2003; Li et al. 2003; Jappsen et al. 2005),

$$T(\rho) = T_0 \begin{cases} 1, & \rho < \rho_0, \\ (\rho/\rho_0)^{2/3}, & \rho_0 \leq \rho \leq \rho_1, \\ (\rho_1/\rho_0)^{2/3}, & \rho > \rho_1, \end{cases} \quad (16)$$

with $T_0 = 20$ K, $\rho_0 = 10^{-14}$ g cm $^{-3}$, and $\rho_1 = 10^{-12}$ g cm $^{-3}$. As is clear from the figures, the barotropic equation of state severely underestimates both the temperature of the gas and the spatial extent of the heated region.

In Figure 12 we show both the ρ - T curve resulting from the Dobbs et al. (2005) barotropic equation of state and also the curve of the optically thin heating and cooling model of Larson (2005)

$$T(\rho) = T_0 \begin{cases} (\rho/\rho_0)^{\gamma_0-1}, & \rho < \rho_0, \\ (\rho/\rho_0)^{\gamma_1-1}, & \rho \geq \rho_0, \end{cases} \quad (17)$$

with $T_0 = 4.4$ K, $\rho_0 = 10^{-18}$ g cm $^{-3}$, $\gamma_0 = 0.73$, and $\gamma_1 = 1.07$. Clearly, this equation of state underestimates the temperature even more severely than the Dobbs et al. barotropic equation of state. For either the Dobbs et al. or Larson equations of state, the Jeans mass in our simulation is larger than the Jeans mass they would predict, often by orders of magnitude. Thus, regardless of the details of how fragmentation occurs, we expect that simulations that adopt either of these proposed equations of state will overpredict the number of fragments. Moreover, both the barotropic and optically thin equations of state produce a range of density with $\gamma \leq 1$ where the thermodynamics favor fragmentation, while our simulation shows that radiation feedback largely prevents this type of thermodynamic behavior.

It is not surprising that the barotropic and optically thin cooling equations of state fare so poorly. As first pointed out by Krumholz (2006b) in a collapsing protostellar core, before nuclear burning starts, the largest energy source either internal or external to the core is the gravitational potential energy released in the final plunge of gas onto the stellar surface. As a result, unless one explicitly includes the energy released by accretion onto the protostellar surface, and the radiative transfer of this energy to the rest of the core, one is ignoring the dominant source of energy in the problem. This is exactly what the barotropic and optically thin approximations do. Our results indicate that this is likely to result in qualitatively incorrect results for fragmentation in massive cores.

Nor can the problem be fixed simply by using better approximate equations of state. As the figures show, the temperature distribution is a function of both time and space and can change in unexpected ways. For example, despite the fact that the luminosity is comparable at 20 kyr to that at 12.5 kyr, and there is more gas heated to moderate temperatures ~ 50 – 100 K, there is actually less mass at temperatures $\gg 100$ K. This is largely because an optically thick disk has formed that is shielding much of the dense gas from protostellar radiation. No equation of state that gives the temperature simply as a function of the density or other local gas properties will reproduce effects like this.

3.4. Disk Properties

Here, we analyze the properties of the disk around the primary star that forms in run 100A, to better understand both angular momentum transport and disk fragmentation. To examine the properties of the disk, we must first isolate it from the background flow. To do so, we choose a density threshold of 10^{-15} g cm $^{-3}$ to separate disk material from the ambient gas. This threshold agrees reasonably well with what one identifies by eye, and values up to a factor of ~ 10 different from this do not produce qualitatively different results. We also focus on gas within 1000 AU of the primary, to ensure that the gas we are examining is in orbit around it rather than around other protostars. After using these

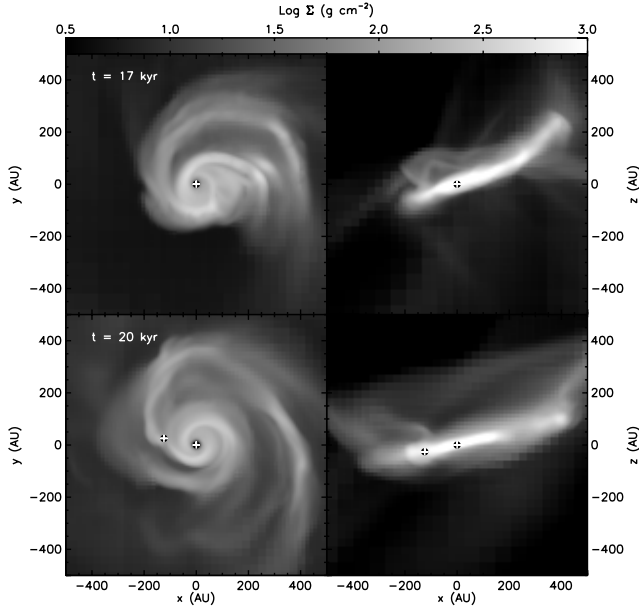


FIG. 13.—Column density of the disk in run 100A at 17 kyr (*top row*) and 20 kyr (*bottom row*), in two orthogonal projections. Stars are indicated by white plus signs. [See the electronic edition of the *Journal* for a color version of this figure.]

criteria to remove extraneous gas, we compute the total angular momentum about the primary of the remaining gas. Since our disk is not aligned with the computational grid, to analyze it we “deproject” by computing the column density Σ , mass-weighted sound speed c_s , and mass-weighted angular velocity Ω projected onto the plane orthogonal to the angular momentum vector. We do this at 17 kyr, just before the first disk fragment forms, and at 20 kyr, the end of our run. The deprojected maps of disk properties at these times form the basis of our analysis. We show the disk at these two times, before deprojection, in Figure 13.

3.4.1. Angular Momentum Transport

First we wish to determine the effective viscosity α for our disks. In a Keplerian disk this is related to the kinematic viscosity ν by $\nu = 2\alpha c_s^2 / (3\Omega)$ (Shakura & Sunyaev 1973). The inward radial drift velocity of the material in the disk is $v_R \approx \nu/R$, and the accretion rate onto the central star is $\dot{M} = 2\pi R \Sigma v_R$, so $\alpha \approx \dot{M} \Omega / (3\pi \Sigma c_s^2)$. We therefore estimate α by computing the mass-weighted average

$$\langle \alpha \rangle \approx \frac{\int_{-\pi}^{\pi} d\phi \int_0^{\infty} dr \Sigma (\dot{M} \Omega) / (3\pi \Sigma c_s^2)}{\int_{-\pi}^{\pi} d\phi \int_0^{\infty} dr \Sigma}. \quad (18)$$

For the properties of our disk at either 17 or 20 kyr, and taking \dot{M} to be the mean accretion rate between these times, $4 \times 10^{-4} M_{\odot} \text{ yr}^{-1}$, we find an effective $\alpha \approx 1.0$ –1.6. This is quite rapid angular momentum transport and is significantly larger than what one expects due to purely local transport phenomena (e.g., Gammie 2001). Accretion is obviously highly time dependent and unsteady, and the disk never settles into a steady state, so the rate of angular momentum transport at any instant may be very different from the average.

To understand the angular momentum transport mechanism, we analyze the spiral pattern in the disk by computing Fourier coefficients of the density distribution in azimuth around the primary star. Defining r as the distance from the primary star in

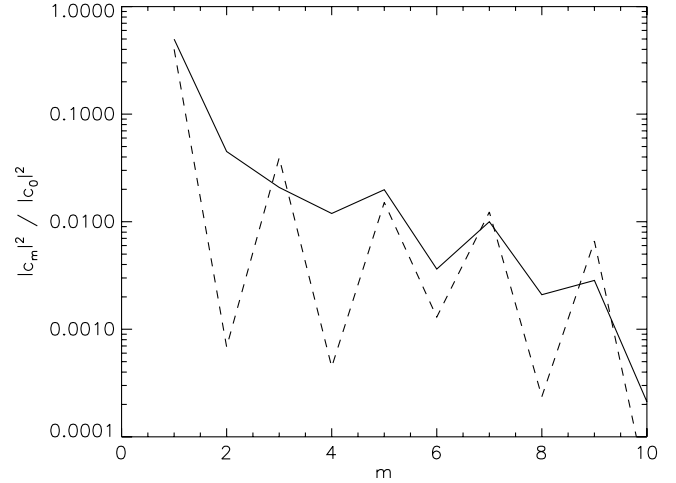


FIG. 14.—Normalized power $|c_m|^2 / |c_0|^2$ in azimuthal mode m in the disk around the primary star at 17 kyr (*solid line*) and 20 kyr (*dashed line*).

our projection and ϕ as an angular coordinate in the projection plane, we compute

$$c_m = \frac{1}{2\pi} \int_{-\pi}^{\pi} d\phi \int_0^{\infty} dr e^{im\phi} r \Sigma(r, \phi). \quad (19)$$

We plot the normalized power $|c_m|^2 / |c_0|^2$ for $m = 1$ –10 in Figure 14. As the figure shows, at both 17 and 20 kyr the vast majority of the power is in the $m = 1$ spiral mode, with smaller amounts of power in other odd modes and very little power in even modes. This suggests that angular momentum transport and spiral arm formation in our disk is primarily due to the SLING instability (Adams et al. 1989; Shu et al. 1990). For disks as massive as ours, $M_d \sim 0.5 M_*$, this mechanism enables accretion on a disk dynamical timescale rather than a viscous timescale, consistent with our value of $\alpha \sim 1$. Angular momentum transport occurs via a global rather than a local instability. Our result is also consistent with previous simulations of gravitational instability in massive disks by Laughlin & Bodenheimer (1994), which show that most power goes into the $m = 1$ mode.

The behavior of disks in our simulations is significantly different than that seen in the simulations of Lodato & Rice (2005) and Rice et al. (2005) who model the evolution of disks with masses ranging from 10% to 100% of the primary object mass using polytropic equations of state with $\gamma > 1$, with added cooling terms that remove energy on timescales from 3 to $13\Omega^{-1}$. They find that for all their runs angular momentum transport is primarily local and that accretion occurs on a viscous rather than a dynamical timescale, with values of $\alpha \leq 0.06$ in all stable disks. When spiral arms form, the majority of the power is in $m = 2$ modes. Disks settle into steady states except when $M_d \gtrsim M_*$.

This difference in behavior is likely to be a real physical effect, caused by two differences between the properties of our disk and those of Lodato & Rice (2005) and Rice et al. (2005). First, the temperature in our disk is set almost entirely by radiative heating and cooling, in contrast to the polytropic plus cooling runs in which disk temperatures are set by the balance between viscous heating and radiative cooling. Viscous heating does not provide enough energy to raise the disk temperature significantly in our run. As a result, the temperature in our disk is almost entirely a function of distance from the primary star, with no significant variation at a given distance due to spiral arms or other density

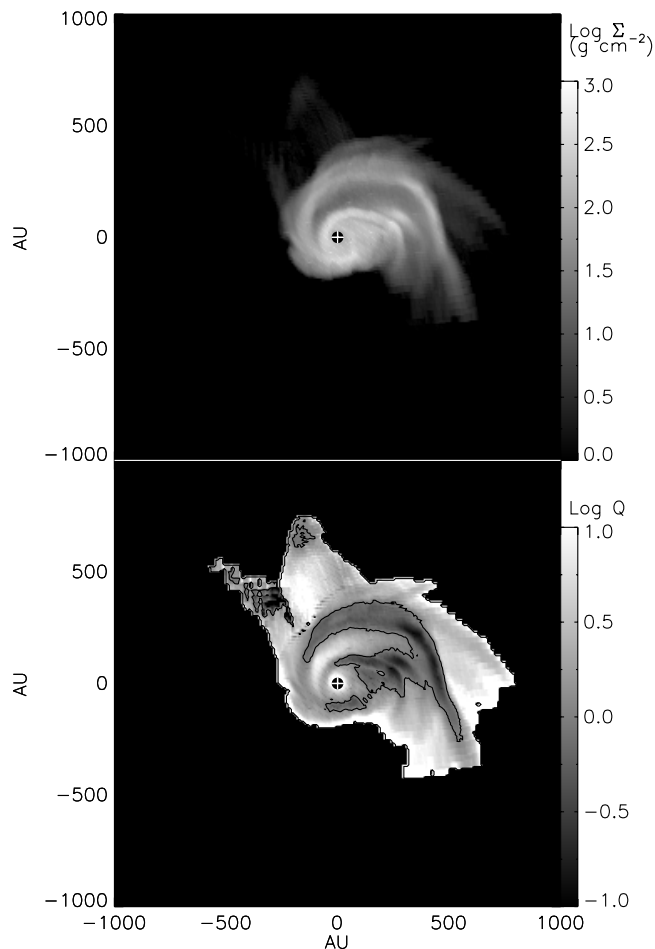


FIG. 15.—Deprojected column density (*top*) and Toomre Q (*bottom*) of the disk around the primary star in run 100A at 17.4 kyr, just as the first disk fragmentation occurs. The positions of stars are indicated by the white plus signs. In the plot of Q , the black contour indicates $Q = 1$, and the exterior black region consists of points for which there is no gas above the density threshold we use to define the edge of the disk. [See the electronic edition of the *Journal* for a color version of this figure.]

or velocity structures in the disk. Consequently, the thermodynamic behavior of our disk is closer to an isothermal equation of state than to the stiffer equations of state produced by values of $\gamma > 1$ and cooling timescales longer than the disk orbital period. This favors the growth of large-scale global modes that produce rapid angular momentum transport, an effect pointed out by Lodato & Rice to explain the differences between their simulations and those of Laughlin & Bodenheimer (1994).

Second, in our simulation the disk is never stable or isolated. The average accretion rate of $4 \times 10^{-4} M_{\odot} \text{ yr}^{-1}$ from 17 to 20 kyr, assuming all mass that reaches the star is processed through the disk, corresponds to $\sim 30\%$ of the disk mass per orbital period. This is obviously a huge perturbation. Most of this accretion comes from a large filament (as shown, for example, in Fig. 4) that is sheared out into a disk as it approaches the protostar, an effect that obviously favors $m = 1$ spiral structure. Partly as a result of this perturbation, our disk is never able to settle into a quasi-steady state, and it forms several fragments. These likely aid in shepherding material inward into the primary star.

These two effects suggest that our results are not inconsistent with the findings of Lodato & Rice (2005) and Rice et al. (2005), simply that our disk is in a different regime of parameter space than they have explored.

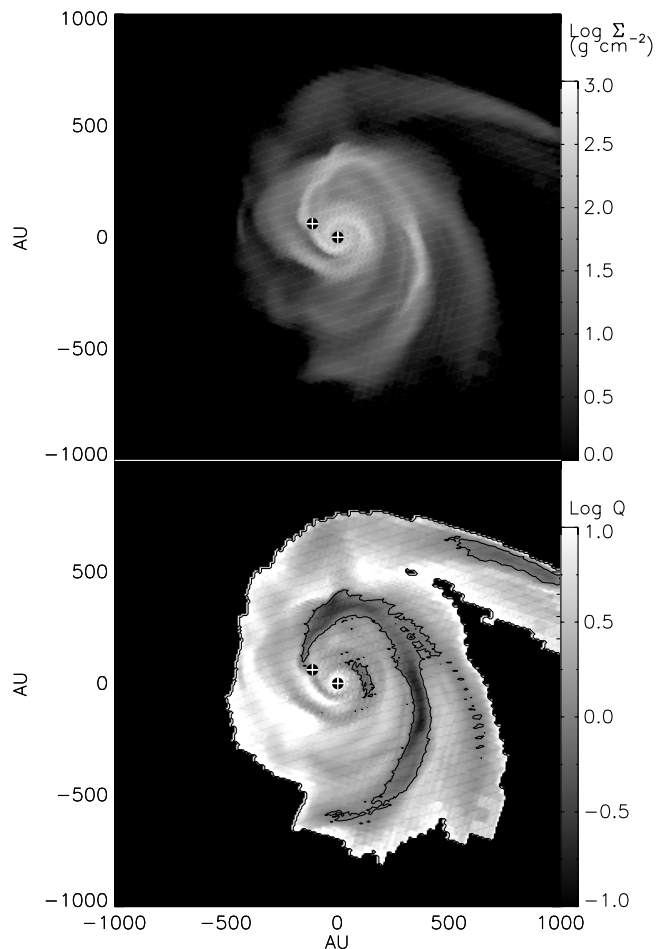


FIG. 16.—Same as Fig. 15, but for run 100A at 20 kyr. [See the electronic edition of the *Journal* for a color version of this figure.]

3.4.2. Disk Fragmentation

To help understand why our disk fragments, we compute the Toomre (1964) parameter

$$Q \approx \frac{\Omega c_s}{\pi G \Sigma}. \quad (20)$$

We do this at each point, and we also compute the mass-weighted azimuthal average,

$$\langle Q \rangle_{\phi}(r) \equiv \frac{\int_{-\pi}^{\pi} d\phi \Sigma(r, \phi) Q(r, \phi)}{\int_{-\pi}^{\pi} d\phi \Sigma(r, \phi)}, \quad (21)$$

as a function of radius. Obviously, this calculation is somewhat approximate, since we do not have a thin, steady, Keplerian disk with a well-defined edge as a background state. Nonetheless, it can give us some insight into the state of the disk and the reason that it fragments.

Figures 15 and 16 show plots of deprojected column density and Q for the disk in run 100A at times of 17 kyr, just before the first fragment forms in the disk, and 20 kyr, when the disk-formed star is still present but there are no other obvious fragments forming, respectively. We show the azimuthally averaged column density and Toomre Q as a function of radius at these two times in Figures 17 and 18. As the plots show, at 17 kyr (Fig. 17) there is a broad region where $Q < 1$, both at individual points and

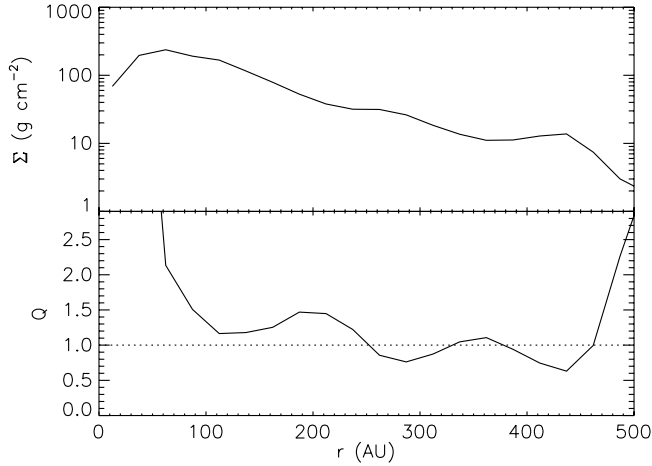


FIG. 17.—Azimuthally averaged column density (*top*) and Toomre Q parameter (*bottom*) as a function of radius in the deprojected protostellar disk at 17 kyr, just before the first disk fragment forms.

in the azimuthal average. This corresponds to the approximate location where the fragment forms. At 20 kyr (Fig. 18), it is clear that there is another region of the disk that has $Q < 1$ at individual points, but there is no region where the azimuthally averaged value of $Q < 1$ (although the ring at 350 AU is extremely close). In general, the disk seems more stable than at 17 kyr, which likely explains why there is no obvious fragment formation at 20 kyr. However, it seems entirely possible that further evolution would decrease Q and lead to additional fragment formation. Although the luminosity of the star will continue to rise as it gains mass, heating the disk, the disk mass will also rise, increasing its shielding against protostellar radiation. It is not clear which of these effects will dominate.

While fragment formation in massive protostellar disks is an interesting phenomenon, it seems unlikely to be a significant hindrance to accretion onto the primary star at this point in the evolution. There is no noticeable drop in the accretion rate onto the primary after 17 kyr, and from 17 to 20 kyr the primary star mass increases by a factor of 6 more than the mass of the embedded fragment. Clearly, most of the mass in the disk is going into the primary, not into disk-formed fragments.

Our findings on disk fragmentation are broadly consistent with the analytic predictions of Kratter & Matzner (2006), who analytically model massive protostellar disks and find that they are unstable to fragmentation at radii $\gtrsim 150$ AU for central stars of mass $M_* \gtrsim 4 M_\odot$. Kratter & Matzner, extending the work of Matzner & Levin (2005), predict that steady state disks should fragment if their sound speeds fall below a critical value $c_{\text{crit}} \approx 1.04(G\dot{M})^{1/3}$, where \dot{M} is the accretion rate onto the star-disk system.

Before applying this condition, we modify it in two ways. First, rather than using the isothermal sound speed to compare to c_{crit} as Matzner & Levin (2005) suggest, we use the adiabatic sound speed because our disks are optically thick to their own radiation. Second, we modify the criterion to account for the fact that angular momentum transport in our disks appears to be due to a global rather than a local gravitational instability. Matzner & Levin and Kratter & Matzner (2006) determine disk stability using the criterion of Gammie (2001), who simulates angular momentum transport by local gravitational instabilities and finds that these produce a maximum effective viscosity $\alpha = 0.23$. The critical sound speed depends on α as $c_{\text{crit}} \propto \alpha^{1/3}$, because α determines

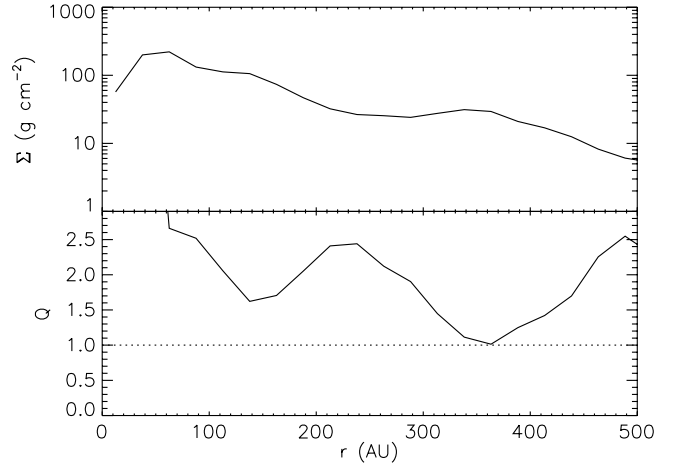


FIG. 18.—Same as Fig. 17, but at 20 kyr.

the rate at which material is processed through the disk onto the central object. Consequently, the increased rate of angular momentum transport in our disks makes disks more stable.

With these two modifications, the Kratter & Matzner (2006) critical temperature for instability to fragment formation becomes

$$T_{\text{crit}} \approx 0.41 \frac{\mu}{\gamma k_B} (\alpha G \dot{M})^{2/3}, \quad (22)$$

$$= 39 \alpha^{2/3} \left(\frac{\dot{M}}{10^{-4} M_\odot \text{ yr}^{-1}} \right)^{2/3} \text{ K}. \quad (23)$$

For the mean accretion rate of $4 \times 10^{-4} M_\odot \text{ yr}^{-1}$ from 17 to 20 kyr and our range of estimates $\alpha = 1.0\text{--}1.6$, this gives $T_{\text{crit}} \approx 70\text{--}100$ K. The temperature in the outer parts of our disks is generally in this range, which explains why they are marginally unstable to fragment formation. It also explains why our typical fragmentation radius is somewhat larger than Kratter & Matzner predict.

4. DISCUSSION

4.1. Discussion of Physical Approximations

Our physical formulation of the problem contains three significant simplifications. Here, we discuss them with the goal of assessing how much they might affect our results.

First, our treatment of radiative transfer, although a significant improvement on previous three-dimensional calculations that ignored radiation entirely, is still quite idealized. Our approach is gray, so we miss effects that arise from the frequency-dependent opacities of dust grains. Preibisch et al. (1995) and Yorke & Sonnhalter (2002), based on two-dimensional calculations, find that, compared to gray, multifrequency calculations generally produce higher dust temperatures and greater degrees of anisotropy in the radiation field. The fact that even with the anisotropy effect, gray radiation almost always underestimates the true temperature suggests that our results on fragmentation are fairly secure, since higher temperatures would further reduce the level of fragmentation. Nonetheless, increasing the anisotropy of the radiation could conceivably leave some parts of the flow cooler than we find, so it would be useful to repeat some of the calculations we present here with a multifrequency radiative transfer code.

In addition to being gray, our radiative transfer approach uses the flux-limited diffusion approximation, which is an approximation

that is only highly accurate in regions that are very optically thick (or that are very optically thin and for which the geometry is simple). Our cores have initial mean surface densities of 0.66 g cm^{-2} , which gives them optical depths $\gtrsim 1$ to infrared photons. Thus, the cores overall are marginally optically thick on average. However, in the dense regions where fragmentation takes place and where it is most important to treat the radiation correctly, surface densities are more typically tens or hundreds of grams per square centimeter. Thus, the regions in which fragmentation occurs are extremely well-described by the diffusion approximation. Thus, we consider it extremely unlikely that our results would change qualitatively if we were to use a more accurate treatment of the radiation field.

A second limitation to our approach is the uncertainty in what our initial and boundary conditions should be, based on our imperfect knowledge of the properties of massive cores and their environments. The MT03 model that we have used fits the data reasonably well, but observations to date reveal only a little about the internal structure of massive cores. The primary uncertainties likely to affect our results are the degree of central concentration, the amount of internal turbulent structure, and the nature of any external perturbations. The first of these is difficult to determine because observations of massive core gas are generally made with interferometers such as the Submillimeter Array (SMA), which remove large-scale power and thus make it difficult to determine quantities like large-scale density gradients. The amount of internal turbulent structure is poorly known observationally simply because of resolution and sensitivity limits. Massive cores are too small for observations to determine fine details of their internal structure. The nature of external perturbations is uncertain because massive cores are embedded within clouds that are themselves turbulent, so rather than providing a constant pressure boundary, the external environment may fluctuate and drive turbulent motions in a massive core.

One might expect that the stronger the central concentration, the less fragmentation will occur. However, nonradiative models produce a great deal of fragmentation, regardless of the initial degree of central concentration, even for cases much more concentrated than the $k_\rho = 1.5$ density gradient we use (e.g., Bate et al. 2003; Goodwin et al. 2004; Dobbs et al. 2005). Thus, the degree of initial concentration in our models seems unlikely to change our results qualitatively. For turbulent density structure, whether it is structure present initially or structure induced by external perturbations on a core's surface, obviously a higher degree of internal structure favors more fragment formation, and massive cores are likely to have some internal structure because they are turbulent. Thus, we do not regard our finding on the absolute number of fragments formed to be definitive for what will happen in real high-mass cores. However, since we use identical initial conditions for the radiative and isothermal runs, the differences between them are likely to remain even for more structured or less concentrated initial density fields. Moreover, the general effect we have found, that radiative heating can shut off collapse to small fragments, while allowing the first object formed to grow to large masses by accreting gas that cannot otherwise collapse, should apply regardless of the initial and boundary conditions. Thus, although the quantitative results may vary for different initial or boundary conditions, the qualitative results that massive cores do not fragment very strongly should be robust.

The third major limitation to our approach is that we have neglected magnetic fields. This simplification is partly justified by observational ignorance. Even in nearby low-mass star-forming regions there is considerable controversy over how dynamically significant magnetic fields are (e.g., Crutcher 1999; Padoan et al.

2004; Tassis & Mouschovias 2004), and observations of more distant, obscured, high-mass star-forming regions are far more difficult. Crutcher (2005) reviews the available data and concludes that magnetic fields are marginally dynamically significant, but this conclusion is highly uncertain due to potential systematic errors in transforming the observed signal into a magnetic field strength (see Krumholz [2006a] for a discussion of this point). Even if magnetic fields are dynamically significant in the initial core, simulations show that turbulence can significantly accelerate the rate of ambipolar diffusion (Heitsch et al. 2004), so the field might diffuse out quickly and have little effect on the overall evolution. Moreover, even if magnetic fields are dynamically important and can modify how fragmentation proceeds, our result that radiative transfer suppresses fragmentation should still hold qualitatively.

A final magnetic effect that could be significant is on our protostellar disks. Since we have no magnetic fields, we obviously have no magnetorotational instability (MRI) and its associated angular momentum transport. It is unclear if the MRI can operate in massive protostellar disks, because their column densities of $\sim 100 \text{ g cm}^{-2}$ may render them so opaque to protostellar ultraviolet radiation that their ionization fractions will be too low for the MRI to operate. (The MRI requires sufficient ionization for the magnetic Reynolds number to be greater than about unity [Sano et al. 1998].) However, if the MRI does operate, its effect should be to increase the rate of angular momentum transport, which will raise the mass of the primary and lower the surface density of our disks, thereby reducing their propensity to fragment. Thus, if anything, we overestimate fragmentation in our radiative runs.

4.2. Numerical Resolution

Another potential concern is whether our results depend on our numerical resolution. At some level, they probably do. The accretion radius around our sink particles is 4 cells, which corresponds to 30 AU in runs 100A, 100B, and 100ISO and 43 AU in run 200A. This means we are unable to resolve binaries whose closest approach is smaller than twice this, and stars that should become tight binaries will instead be merged in our code. However, given that except in the isothermal run, the amount of mass gained by mergers is negligible, this effect cannot be significant in setting the primary star mass. We are also insensitive to the formation of fragments on scales smaller than the accretion radius, so we could conceivably underpredict the number of fragments. In our radiative runs, this is unlikely to be a problem, because, as Figure 11 shows, all the gas within ~ 30 AU of the primary protostar is heated to $\gtrsim 300$ K, even at very early times. Thus, heating should very strongly suppress fragment formation there. On the other hand, this effect could be very significant in the isothermal run, since isothermal calculations with higher resolution than we have used do find significant amounts of fragment formation on $\lesssim 100$ AU scales (e.g., Bate et al. 2003; Dobbs et al. 2005), and simulations with varying resolution find that the amount of fragmentation and the mean fragment mass are resolution-dependent (Martel et al. 2006).

A related concern is that we might be missing fragmentation in our disks due to excessive numerical viscosity. Our Cartesian grid produces a numerical viscosity that gives an effective α of (Krumholz et al. 2004)

$$\alpha \approx 78 \frac{r_B}{\Delta x} \left(\frac{r}{\Delta x} \right)^{-3.85}, \quad (24)$$

$$\approx 0.72 \Delta x_{7.5}^{-2.85} M_1 T_{100}^{-1} \left(\frac{r}{100 \text{ AU}} \right)^{-3.85}, \quad (25)$$

where r is the distance from the star about which the disk orbits, the mass of the star in solar masses is M_1 , the disk temperature in units of 100 K is T_{100} , and $\Delta x_{7.5}$ is the grid spacing in units of 7.5 AU. This means that at distances ~ 300 AU, where much of the disk mass resides, our typical numerical α is of order 10^{-2} , insignificant compared to that induced by the SLING instability. On scales $\lesssim 100$ AU, however, numerical viscosity is probably significant in shaping the evolution of our disks and may inhibit fragment formation. This problem, to the extent that it is significant, almost certainly affects the isothermal run more than the others, since irradiated disks at such small radii are quite hot and thus resistant to fragmentation. The problem may also be more severe in run 200A, where the larger cell size means that the untrustworthy region is a factor of 2–3 larger. This may explain the reduced disk fragmentation we find in that run.

4.3. Implications for Massive Star Formation

One of the outstanding problems in massive star formation has been how to gather enough mass to make a massive star. Our simulations, coupled with other recent work, suggest that we may be nearing a solution. Observations now unambiguously reveal that there are massive, centrally concentrated cores (e.g., see review by Garay 2005). How these cores form is a topic of active research (e.g., Padoan & Nordlund 2002; Tilley & Pudritz 2004; Li et al. 2004), but since we can determine massive core properties from observation, we need not solve this problem to model their evolution.

While it is appealing to see massive cores as the progenitors of massive stars, one might legitimately worry that these objects fragment to produce large numbers of low-mass stars rather than a few massive stars. Some of these low-mass stars could possibly gain mass via competitive accretion of gas (Bonnell et al. 2001a, 2001b, 2004) or via stellar collisions (Bonnell et al. 1998; Bonnell & Bate 2005), becoming massive stars. However, the former mechanism seems not to work unless star clusters are typically subvirial globally collapsing objects (Krumholz et al. 2005c; Bonnell & Bate 2006; Krumholz 2006a), which appears to be ruled out by observations of the star formation rate and age spread in young clusters (Tan et al. 2006; Krumholz & Tan 2007). The latter possibility requires stellar densities that would be very difficult to achieve without global collapse and that are orders of magnitude larger than the highest observed stellar densities in young clusters.

Our results suggest that the solution to this dilemma is that massive stars do form directly from the collapse of massive cores (MT03) and that these cores do not fragment strongly because radiation feedback effectively shuts off fragmentation (Krumholz 2006b). In a massive collapsing core, most of the mass goes into one primary object. Thus, massive cores, objects that we know exist from observations, are the direct progenitors of massive stars, with no need for intermediate steps of competitive accretion or collisions.

In this work we have not addressed the question of whether, at higher masses, radiation pressure might halt accretion and thereby prevent massive cores from making massive stars. However, theoretical work to date suggests that radiation beaming by a combination of protostellar outflow cavities, the protostellar disk, and the accreting envelope (Yorke & Sonnhalter 2002; Krumholz et al. 2005a, 2005b) provide a robust mechanism for allowing accretion to continue in the face of radiation pressure. We plan to report on three-dimensional radiation-hydrodynamic simulations of this problem in future work.

4.4. Implications for Future Simulations

Our results show definitively that radiative transfer significantly modifies the manner in which accretion and fragmenta-

tion occur in the environments where massive stars form, at least on the size scales of individual cores. The effective heating radius is >1000 AU even before nuclear burning starts in any protostar, simply due to accretion luminosity. Once nuclear burning starts, the heating radius will rise rapidly, since the luminosity rises as roughly M^3 . It is not possible to capture this effect simply by using a modified equation of state, because the heating process depends on the radiative transfer of energy from gas falling onto protostellar surfaces to gas in the surrounding envelope. We conclude that simulations of massive star formation and star cluster formation that do not include radiative transfer and accretion luminosity are not reliable on size scales below several thousand AU and that such calculations almost certainly overestimate the amount of fragmentation that occurs. This is true even before any of the stars formed begin nuclear burning. If one wishes to continue a simulation to the point where deuterium burning starts, one must include that effect as well.

A critical question, which our work raises but does not address, is the extent to which the overfragmentation problem affects simulations of low-mass star formation. In such environments cores are usually separated by more than 1000 AU, accretion rates and the resulting accretion luminosities are lower, and lower column densities produce lower opacities to what radiation there is. Thus, we expect the effect on fragmentation to be less severe than we have found. Nonetheless, it seems likely that there will be some effect, particularly for models in which brown dwarfs or low-mass stars form by disk fragmentation (e.g., Bate et al. 2002, 2003; Goodwin et al. 2004) and for competitive accretion models in which numerous brown dwarfs or low-mass stars form in clusters $\lesssim 1000$ AU in size and then evolve in a manner dictated largely by N -body interactions (Bate & Bonnell 2005; Bonnell & Bate 2005). In particular, Matzner & Levin (2005) argue that radiative transfer effects are likely to prevent the formation of brown dwarfs by disk fragmentation, and our results support the idea that this effect might be important. It is therefore critical to repeat these calculations with radiative transfer to see if the fragments persist once better physics is included, a point also made by Whitehouse & Bate (2006).

5. CONCLUSION

We report the results of simulations of the collapse and fragmentation of massive protostellar cores using gravito-radiation hydrodynamics with adaptive mesh refinement. We find that including radiative transfer in our simulations produces dramatic effects on the evolution of these objects. When radiation is included, massive protostellar cores with the properties of observed cores do not fragment strongly. They collapse to a handful of objects, with the majority of the mass accreting onto one primary object. The object gains mass by accretion of gas that is prevented from collapsing by radiative heating. Some low-mass stars do form in addition to the primary massive star, through a combination of fragmentation at sites sufficiently far from the protostar to be fairly cool, and fragmentation of unstable protostellar disks around the massive star. However, these do not contain significant mass. The disks that form are able to transport mass onto the central star very rapidly due to a large-scale gravitational instability, which appears to form due to the SLING mechanism. Overall, our results are consistent with the turbulent core model of MT02 and MT03, with the analytic treatment of radiative suppression of fragmentation by Krumholz (2006b) and with the analytic massive protostellar disk models of Kratter & Matzner (2006).

Our results suggest that massive cores are the direct progenitors of massive stars, without an intermediate phase of

competitive accretion or stellar collisions. Both of these mechanisms require that a large number of protostars form out of dense gas in clusters ~ 1000 AU in size or smaller. However, such strong fragmentation seems not to occur in the environments where massive stars form, because rapid accretion rapidly raises the gas temperature and prevents nucleation of small protostars. Instead, most gas in a massive core accretes onto the first object to form, and this object prevents other, comparable-mass stars from forming after it.

One additional conclusion from our work is that one must include radiative transfer in simulations in order to obtain the correct behavior on small scales. Prescriptions for the equation of state based on the barotropic approximation or on optically thin heating and cooling models severely underestimate gas temperatures, because they do not and cannot include heating by accretion luminosity onto a central protostar. The high densities found in massive protostellar cores mean that this luminosity can reach thousands of solar luminosities even for $\lesssim 1 M_{\odot}$ protostars, an effect that cannot be neglected.

We thank K. M. Kratter, S. S. R. Offner, C. D. Matzner, R. T. Fisher, J. M. Stone, and J. C. Tan for helpful discussions. Support for this work was provided by NASA through Hubble Fellowship grant HSF-HF-01186 awarded by the Space Telescope Science Institute, which is operated by the Association of Universities for Research in Astronomy, Inc., for NASA, under contract NAS 05-26555 (M. R. K.); NASA ATP grants NAG 05-12042 and NNG 06-GH96G (R. I. K. and C. F. M.); the US Department of Energy at the Lawrence Livermore National Laboratory under contract W-7405-Eng-48 (R. I. K.); and the NSF through grants AST 00-98365 and AST 06-06831 (C. F. M.). This research was also supported by grants of high-performance computing resources from the Arctic Region Supercomputing Center; the NSF San Diego Supercomputer Center through NPACI program grant UCB267; the National Energy Research Scientific Computing Center, which is supported by the Office of Science of the US Department of Energy under Contract DE-AC03-76SF00098, through ERCAP grant 80325; and the US Department of Energy at the Lawrence Livermore National Laboratory under contract W-7405-Eng-48.

REFERENCES

- Adams, F. C., Ruden, S. P., & Shu, F. H. 1989, *ApJ*, 347, 959
 Banerjee, R., Pudritz, R. E., & Anderson, D. W. 2006, *MNRAS*, 373, 1091
 Bate, M. R., & Bonnell, I. A. 2005, *MNRAS*, 356, 1201
 Bate, M. R., Bonnell, I. A., & Bromm, V. 2002, *MNRAS*, 332, L65
 ———. 2003, *MNRAS*, 339, 577
 Bell, J., Berger, M. J., Saltzman, J., & Welcome, M. 1994, *SIAM J. Sci. Comp.*, 15, 127
 Berger, M. J., & Collela, P. 1989, *J. Comp. Phys.*, 82, 64
 Berger, M. J., & Olinger, J. 1984, *J. Comp. Phys.*, 53, 484
 Beuther, H., & Schilke, P. 2004, *Science*, 303, 1167
 Beuther, H., Sridharan, T. K., & Saito, M. 2005, *ApJ*, 634, L185
 Beuther, H., Zhang, Q., Sridharan, T. K., Lee, C.-F., & Zapata, L. A. 2006, *A&A*, 454, 221
 Bonnell, I. A., & Bate, M. R. 2005, *MNRAS*, 362, 915
 ———. 2006, *MNRAS*, 624
 Bonnell, I. A., Bate, M. R., Clarke, C. J., & Pringle, J. E. 2001a, *MNRAS*, 323, 785
 Bonnell, I. A., Bate, M. R., & Zinnecker, H. 1998, *MNRAS*, 298, 93
 Bonnell, I. A., Clarke, C. J., & Bate, M. R. 2006, *MNRAS*, 368, 1296
 Bonnell, I. A., Clarke, C. J., Bate, M. R., & Pringle, J. E. 2001b, *MNRAS*, 324, 573
 Bonnell, I. A., & Davies, M. B. 1998, *MNRAS*, 295, 691
 Bonnell, I. A., Vine, S. G., & Bate, M. R. 2004, *MNRAS*, 349, 735
 Carey, S. J., Feldman, P. A., Redman, R. O., Egan, M. P., MacLeod, J. M., & Price, S. D. 2000, *ApJ*, 543, L157
 Crutcher, R. M. 1999, *ApJ*, 520, 706
 ———. 2005, in *IAU Symp. 227, Massive Star Birth*, ed. R. Cesaroni et al. (Cambridge: Cambridge Univ. Press), 98
 Dobbs, C. L., Bonnell, I. A., & Clark, P. C. 2005, *MNRAS*, 360, 2
 Dubinski, J., Narayan, R., & Phillips, T. G. 1995, *ApJ*, 448, 226
 Elmegreen, B. G., & Krakowski, A. 2001, *ApJ*, 562, 433
 Fisher, R. T. 2002, Ph.D. thesis, Univ. California, Berkeley
 Gammie, C. F. 2001, *ApJ*, 553, 174
 Garay, G. 2005, in *IAU Symp. 227, Massive Star Birth*, ed. R. Cesaroni et al. (Cambridge: Cambridge Univ. Press), 86
 Goodwin, S. P., Whitworth, A. P., & Ward-Thompson, D. 2004, *A&A*, 414, 633
 Hayes, J. C., Norman, M. L., Fiedler, R. A., Bordner, J. O., Li, P. S., Clark, S. E., ud-Doula, A., & Mac Low, M.-M. 2006, *ApJS*, 165, 188
 Heitsch, F., Zweibel, E. G., Slyz, A. D., & Devriendt, J. E. G. 2004, *ApJ*, 603, 165
 Hillenbrand, L. A., & Hartmann, L. W. 1998, *ApJ*, 492, 540
 Howell, L. H., & Greenough, J. A. 2003, *J. de Chim. Phys.*, 184, 53
 Huff, E. M., & Stahler, S. 2006, *ApJ*, 644, 355
 Jappsen, A.-K., Klessen, R. S., Larson, R. B., Li, Y., & Mac Low, M.-M. 2005, *A&A*, 435, 611
 Johnstone, D., Fich, M., Mitchell, G. F., & Moriarty-Schieven, G. 2001, *ApJ*, 559, 307
 Klein, R. I. 1999, *J. Comp. Appl. Math.*, 109, 123
 Kratter, K. M., & Matzner, C. D. 2006, *MNRAS*, 373, 1563
 Krumholz, M. R. 2006a, in *Massive Stars: From Pop III and GRBs to the Milky Way*, Proceedings of the 2006, STScI May Symp., in press (astro-ph/0607429)
 ———. 2006b, *ApJ*, 641, L45
 Krumholz, M. R., Klein, R. I., & McKee, C. F. 2005a, in *IAU Symp. 227, Massive Star Birth*, ed. R. Cesaroni et al. (Cambridge: Cambridge Univ. Press), 231
 ———. 2007, *ApJS*, submitted (astro-ph/0611003)
 Krumholz, M. R., McKee, C. F., & Klein, R. I. 2004, *ApJ*, 611, 399
 ———. 2005b, *ApJ*, 618, L33
 ———. 2005c, *Nature*, 438, 332
 Krumholz, M. R., & Tan, J. C. 2007, *ApJ*, 654, 304
 Larson, R. B. 2005, *MNRAS*, 359, 211
 Laughlin, G., & Bodenheimer, P. 1994, *ApJ*, 436, 335
 Li, P. S., Norman, M. L., Mac Low, M.-M., & Heitsch, F. 2004, *ApJ*, 605, 800
 Li, Y., Klessen, R. S., & Mac Low, M.-M. 2003, *ApJ*, 592, 975
 Lodato, G., & Rice, W. K. M. 2005, *MNRAS*, 358, 1489
 Martel, H., Evans, II, N. J., & Shapiro, P. R. 2006, *ApJS*, 163, 122
 Masunaga, H., & Inutsuka, S. 2000, *ApJ*, 531, 350
 Masunaga, H., Miyama, S. M., & Inutsuka, S. 1998, *ApJ*, 495, 346
 Matzner, C. D., & Levin, Y. 2005, *ApJ*, 628, 817
 McKee, C. F., & Tan, J. C. 2002, *Nature*, 416, 59 (MT02)
 ———. 2003, *ApJ*, 585, 850 (MT03)
 Menten, K. M., Pillai, T., & Wyrowski, F. 2005, in *IAU Symp. 227, Massive Star Birth*, ed. R. Cesaroni et al. (Cambridge: Cambridge Univ. Press), 23
 Motte, F., Andre, P., & Neri, R. 1998, *A&A*, 336, 150
 Mueller, K. E., Shirley, Y. L., Evans, N. J., & Jacobson, H. R. 2002, *ApJS*, 143, 469
 Nakano, T., Hasegawa, T., Morino, J., & Yamashita, T. 2000, *ApJ*, 534, 976
 Nakano, T., Hasegawa, T., & Norman, C. 1995, *ApJ*, 450, 183
 Onishi, T., Mizuno, A., Kawamura, A., Tachihara, K., & Fukui, Y. 2002, *ApJ*, 575, 950
 Padoan, P., Jimenez, R., Juvela, M., & Nordlund, Å. 2004, *ApJ*, 604, L49
 Padoan, P., & Nordlund, Å. 2002, *ApJ*, 576, 870
 Palla, F., & Stahler, S. W. 1992, *ApJ*, 392, 667
 Pillai, T., Wyrowski, F., Carey, S. J., & Menten, K. M. 2006, *A&A*, 450, 569
 Plume, R., Jaffe, D. T., Evans, N. J., Martin-Pintado, J., & Gomez-Gonzalez, J. 1997, *ApJ*, 476, 730
 Pollack, J. B., Hollenbach, D., Beckwith, S., Simonelli, D. P., Roush, T., & Fong, W. 1994, *ApJ*, 421, 615
 Preibisch, T., Sonnhalter, C., & Yorke, H. W. 1995, *A&A*, 299, 144
 Puckett, E. G., & Saltzman, J. S. 1992, *Physica D*, 60, 84
 Rathborne, J. M., Jackson, J. M., Chambers, E. T., Simon, R., Shipman, R., & Frieswijk, W. 2005, *ApJ*, 630, L181
 Rathborne, J. M., Jackson, J. M., & Simon, R. 2006, *ApJ*, 641, 389
 Reid, M. A., & Wilson, C. D. 2005, *ApJ*, 625, 891
 ———. 2006a, *ApJ*, 644, 990
 ———. 2006b, *ApJ*, 650, 970
 Rice, W. K. M., Lodato, G., & Armitage, P. J. 2005, *MNRAS*, 364, L56
 Salpeter, E. E. 1955, *ApJ*, 121, 161
 Sano, T., Inutsuka, S.-I., & Miyama, S. M. 1998, *ApJ*, 506, L57
 Shakura, N. I., & Sunyaev, R. A. 1973, *A&A*, 24, 337
 Shirley, Y. L., Evans, N. J., Young, K. E., Knez, C., & Jaffe, D. T. 2003, *ApJS*, 149, 375
 Shu, F. H., Tremaine, S., Adams, F. C., & Ruden, S. P. 1990, *ApJ*, 358, 495
 Simon, R., Jackson, J. M., Rathborne, J. M., & Chambers, E. T. 2006, *ApJ*, 639, 227
 Sridharan, T. K., Beuther, H., Saito, M., Wyrowski, F., & Schilke, P. 2005, *ApJ*, 634, L57

- Stahler, S. W. 1988, *ApJ*, 332, 804
- Stanke, T., Smith, M. D., Gredel, R., & Khanzadyan, T. 2006, *A&A*, 447, 609
- Tan, J. C., Krumholz, M. R., & McKee, C. F. 2006, *ApJ*, 641, L121
- Tassis, K., & Mouschovias, T. C. 2004, *ApJ*, 616, 283
- Testi, L., & Sargent, A. I. 1998, *ApJ*, 508, L91
- Tilley, D. A., & Pudritz, R. E. 2004, *MNRAS*, 353, 769
- Toomre, A. 1964, *ApJ*, 139, 1217
- Toro, E. 1997, *Riemann Solvers and Numerical Methods for Fluid Dynamics: A Practical Introduction* (Berlin: Springer)
- Truelove, J. K., Klein, R. I., McKee, C. F., Holliman, J. H., Howell, L. H., & Greenough, J. A. 1997, *ApJ*, 489, L179
- Truelove, J. K., Klein, R. I., McKee, C. F., Holliman, J. H., Howell, L. H., Greenough, J. A., & Woods, D. T. 1998, *ApJ*, 495, 821
- Whitehouse, S. C., & Bate, M. R. 2006, *MNRAS*, 367, 32
- Yorke, H. W., & Bodenheimer, P. 1999, *ApJ*, 525, 330
- Yorke, H. W., & Sonnhalter, C. 2002, *ApJ*, 569, 846